

© Copyright by Abdullah Bilal 2016

All Rights Reserved

An Investigation of Static and Dynamic Data Using Multistage Triaxial Tests

A Thesis

Presented to

the Department of Petroleum Engineering

University of Houston

In Partial Fulfillment

of the Requirements for the Degree

Master of Science

By

Abdullah Bilal

May 2016

An Investigation of Static and Dynamic Data Using Multistage Triaxial Tests

Abdullah Bilal

Approved:

Chair of the Committee,
Dr. Michael Myers, Associate
Professor, Cullen College of
Engineering

Committee Members:

Dr. Lori Hathon, Associate
Professor, Petroleum Engineering
Department

Dr. John Dudley
Subject matter expert for
experimental core analysis, Shell
international E&P.

Dr. Suresh K. Khator, Associate Dean, Cullen
College of Engineering

Dr. Tom Holley, Professor and
Director, Petroleum Engineering
Department

Acknowledgements

I would like to express my gratitude to my committee chair, Dr. Michael Myers. I really appreciate his intellectual skills and experience which have added positively to my graduate experience. I would not have been able to complete this thesis without his encouragement and effort. Special thanks to my advisor, Dr. Lori Hathon, who has provided me with guidance that I needed to complete this thesis. I feel very honored to have her on my committee.

I am very thankful to Dr. John Dudley, whose vast expertise and knowledge in experimental rock mechanics provided an invaluable input to my thesis. I really appreciate his guidance and support. It has been a great honor to have him as a committee member.

I would like to thank my lab mates for their support. Mohab Dessouki for his help in taking experimental data and Malik Alsalman for helping me in processing the data.

An Investigation of Static and Dynamic Data Using Multistage Triaxial Tests

An Abstract

of a

Thesis

Presented to

the Department of Petroleum Engineering

University of Houston

In Partial Fulfillment

of the Requirements for the Degree

Master of Science

By

Abdullah Bilal

May 2016

Abstract

The focus of this work is to develop an improved understanding of the relationship between static and dynamic data. “Static” data is defined as the large strain ($> 10^{-3}$) measurements on the unloading and reloading tri-axial stress paths. The “Dynamic” data is the small strain ($< 10^{-6}$) data acquired using standard acoustic velocity measurement techniques. Comparisons are made for both Young’s modulus and Poisson’s ratio along these stress paths. Quadratic fits have been applied to the static data on both the unloading and reloading cycles. This allows us to separate the elastic response into a linear elastic term, M_1 , and a nonlinear elastic term the “hypermodulus”, M_2 . M_1 is interpreted to be dominated by the stiffness of the grain contacts and follow a Hertzian contact model. It is shown to increase linearly with deviatoric stress and independent of confining stress for both the unloading and reloading cycles. The magnitude of M_2 is attributed to the opening and closing of compliant pores and decreases with increasing confining stress. This interpretation for M_2 results from the correlations we find between the nonlinear term and the irrecoverable strains. To our knowledge this is the first time the physical mechanisms behind the static and dynamic elastic responses have been isolated.

Table of Contents

Acknowledgements.....	v
Abstract.....	vii
Table of Contents.....	viii
Table of Figures.....	x
Table of Table.....	xiv
Chapter 1: Introduction.....	1
Chapter 2: Background.....	2
2.1 The Stress-Strain Curve.....	2
2.2 Deviatoric Stress.....	4
2.3 Strain and its Relation to the Point of Positive Dilatancy.....	4
2.2 Modulus.....	6
Chapter 3 Experimental Equipment and Data Analysis.....	7
3.1 Lab Equipment.....	7
3.2 Triaxial Tests.....	9
3.3 Multistage Triaxial test.....	9
3.4 Experimental Error.....	12
3.5 Dynamic Data.....	12
3.6 Quadratic Fits to the Static Data.....	13
3.7 Measurement of Irrecoverable Strains.....	16
Chapter 4 Data Analysis.....	17
4.1 Berea Sandstone.....	17
4.1.1 Comparison of Static and Dynamic Young's Modulus.....	19
4.1.2 Berea small strain modulus (M_1).....	21
4.1.3 Berea Hypermodulus.....	22
4.1.4 Berea Poisson's ratio.....	23
4.1.5 Berea - Irrecoverable strain.....	24
4.2 Castlegate.....	25

4.2.1 Comparison of Static and Dynamic Young's Modulus	27
4.2.2 Castlegate Young's modulus	30
4.2.3 Castlegate Hypermodulus	30
4.2.4 Castlegate - Poisson's ratio	31
4.2.5 Castlegate Irrecoverable strain.....	31
4.3 Austin Chalk.....	32
4.3.1 Static and Dynamic Young's Modulus - Austin Chalk	34
4.3.3 Austin Chalk Small Strain Young's Modulus	36
4.3.4 Austin Chalk Hypermodulus.....	36
4.3.5 Austin Chalk Poisson's Ratio	37
4.3.5 Austin Chalk Irrecoverable Strains.....	37
4.4 Dundee Sandstone	38
4.4.1 Interpretation of Static and Dynamic Young's Modulus Measurements.....	40
4.4.2 Dundee small strain young's modulus (M_1)	40
4.4.3 Dundee Hypermodulus	41
4.4.5 Dundee Irrecoverable Strains.....	42
Chapter 5 - Results.....	43
5.1 Hypermodulus versus confining pressure	43
5.2 Summary plot for M_1	43
5.3 Relation between irrecoverable strain and hypermodulus	44
5.3 Conceptual Model	45
5.4 Conclusions	47
Chapter 6 Appendix	48
6.1 Berea Tabulated Data	48
6.2 Castlegate	52
6.3 Austin Chalk Tabulated Data	58
6.4 Dundee Tabulated Data.....	61
Bibliography	63

Table of Figures

Figure 2.1: Typical stress-strain behavior of a rock under increasing axial stress. The three regions exhibited are defined by the magnitudes of the recoverable and irrecoverable strains. S is the slope of the stress strain curve and referred to as the sample stiffness. If the region is assumed to be elastic, the stiffness is equal to Young's modulus (E).	3
Figure 2.2: Deviatoric stress versus volumetric strain showing the point of positive dilatancy (PPD) where volumetric strain changes from increasing to decreasing. The tangent to the curve is vertical.	5
Figure 3.1: The sample mounting and measurement assembly with LVDTs and cantilever bridge and acoustic endcaps. The average of the axial and radial measurements is used. .	7
Figure 3.2: The cylindrical pressure vessel in which the sample assembly is placed. The maximum pressure is 12000 psi which is applied by displacement pumps under PID (proportional integral differential) control.....	8
Figure 3.3: Experimental setup including the computerized control panel. The entire apparatus is PID controlled and capable of 75000 lb. axial load and 12000 psi confining stress.....	8
Figure 3.4: Data for a typical triaxial test. The deviatoric stress is plotted on the vertical axis. Axial strain is plotted on the horizontal axis. This is a conventional triaxial test where the confining stress is held constant throughout.	9
Figure 3.5: Stress path for multistage triaxial test showing deviatoric stress on y-axis and axial strain on x-axis. The red curve is taken at a lower confining pressure than the blue curve. The sample is unloaded at the point of positive dilatancy.	11
Figure 3.6: A typical quadratic fit for deviatoric stress versus strain for Austin Chalk at 5000 psi confining stress on the loading stress path. This fit is within the expected error.	14
Figure 3.7: M_1 and M_2 values obtained by fitting portions of the reloading curve. As the percentage of the curve is increased, M_1 is constant but M_2 is constant only when one quarter or one half of the reloading curve is fit. The value of M_2 is determined from the portion of the curve where the value is stable.....	15
Figure 3.8: Confining stress versus strain for the MST test for Austin Chalk. Each horizontal line is a cycle of the loading and unloading of the sample. The vertical lines are due to the increase of 1500 psi in the confining stress. The percent irrecoverable stain is the irrecoverable strain normalized to the total strain at each confining stress.....	16
Figure 4.1: The pretest and post test sample pictures. The sample is stored in a Viton sleeve post test to keep it intact. This sample exhibited a brittle failure.	17

Figure 4.2: Multistage triaxial test results for Berea showing axial, radial and volumetric strains as function of deviatoric stress. The strains are zeroed at each confining pressure. The slight dips in the data are due to creep effects that occur when the axial loading is halted for the velocity measurement. 18

Figure 4.3: The single stage triaxial tests for Berea showing the axial, radial and volumetric strains as function of deviatoric stress. Each of these tests was run on a separate sample. The effects of sample twinning are also evident when compared to Figure 4.2 19

Figure 4.4: Static and dynamic YM versus strain on loading and unloading stress path respectively for different confining pressure. Static and dynamic Young's modulus (M_1) are equal at low strain. 20

Figure 4.5a, b: Static vs Dynamic small strain modulus on loading and unloading stress path respectively showing they are both equal within experimental error. 22

Figure 4.6 a, b: Hyper modulus versus confining pressure for both loading and unloading stress path. M_2 decreases with increasing confining pressure. This is due to the effect of cracks closing..... 22

Figure 4.7 a, b: Berea Poisson's ratio on loading and unloading stress path respectively for different confining pressures. Poisson's ratio is near zero at the beginning of the cycles and approaches the dynamic value at the end. The points in black are interpreted to be on the initial loading curve..... 23

Figure 4.8: The Berea confining pressure versus axial strain. The average value of 5% was obtained. This was the lowest measured value of irrecoverable strain..... 24

Figure 4.9: Castlegate post and pretest sample pictures. The posttest sample is kept in a Viton sleeve to keep it intact. This sample exhibited a brittle failure..... 25

Figure 4.10: Fountain plot for Castlegate showing axial, confining and radial strains. At lower confining pressure the slope is sensitive to confining pressure but for higher confining pressures the slope is almost constant. 26

Figure 4.11: The p/q plot for multistage triaxial test for Castlegate showing friction angle of 30.4° and 1192 psi cohesion. Sig1 and Sig3 are axial and radial stress respectively. . 27

Figure 4.12: Static and dynamic Young's modulus versus strain on loading and unloading stress paths. Similar to Berea the static modulus decreases whereas dynamic modulus increases with increasing deviatoric stress. Very good agreement is obtained between the static and dynamic data at low strains..... 28

Figure 4.13 a, b: The Static data for 1000, 2000 and 3000 psi confining pressures on both loading and unloading stress path. We did not obtain dynamic data due to equipment failure. 29

Figure 4.14 a, b: Static versus dynamic small strain modulus on the loading and unloading stress path. They are equal within experimental error. The values are tabulated in appendix.....	30
Figure 4.15 a, b: Hypermodulus versus confining pressure on both loading and unloading stress path. The value of M_2 (degree of nonlinearity of Young's modulus) decreases with increasing confining pressure.	30
Figure 4.16 a, b: Castlegate Poisson's ratio on the loading and unloading stress path. Dynamic Poisson's ratio is constant whereas static is small at the beginning of unload and reload cycle and it increases as the cycle progresses.....	31
Figure 4.17: The confining pressure vs axial strain. The value of irrecoverable strain is approximately 16%.	31
Figure 4.18: Austin chalk pretest and posttest sample picture. This sample exhibited a ductile failure.	32
Figure 4.19: The Fountain plot for the multistage test performed on Austin Chalk showing radial, axial and volumetric strains. The sample exhibited very ductile behavior near the PPD.	33
Figure 4.20: The p/q plot for Austin Chalk, the friction angle is 22.1 degrees and the measured cohesion is 2154 psi. Due to the ductile nature of this material the actual cohesion may be much lower (nonlinear yield criteria).....	33
Figure 4.21 a, b: Static and dynamic Young's modulus versus strain on loading and unloading stress paths. The moduli at the beginning of the unloading stress path cross. This is interpreted as the effects of creep.....	35
Figure 4.22 a, b: The static versus dynamic small strain modulus on loading and unloading stress paths. Both the moduli are equal to each other within the experimental error.....	36
Figure 4.23 a, b: Hypermodulus vs confining pressure for loading and unloading stress path.....	36
Figure 4.24 a, b: Austin Chalk Poisson's ratio on loading and unloading stress path respectively plotted for different confining pressures.	37
Figure 4.25: Confining pressure vs axial strain to calculate irrecoverable strains directly. The measured value of irrecoverable strain is 75%.	37
Figure 4.26: Posttest and pretest sample picture. The sample is kept in viton sleeve post test to keep it intact. The slip surface is evident in the post test picture. This sample exhibited a brittle behavior.	38
Figure 4.27: Fountain plot for multistage tri-axial test for Dundee.....	39
Figure 4.28: Mohr Coulomb plot for Dundee showing friction angle of 54.8 deg and 222.3 psi cohesion.....	39

Figure 4.29 a, b: Static and dynamic Young's modulus versus strain on loading and unloading stress paths.	40
Figure 4.30 a, b: The static versus dynamic moduli on the loading and unloading stress path.....	41
Figure 4.31 a, b: Hypermodulus vs confining pressure for loading and unloading cycle respectively	41
Figure 4.32 Confining pressure vs axial strain to calculate irrecoverable strains directly	42
Figure 5.1: a, b Hyper modulus vs confining pressure for all the samples.....	43
Figure 5.2: Static M1 vs dynamic M1 for all the rocks. They are equal within experimental error.....	44
Figure 5.3: Comparison of M1 obtained from quadratic fits vs M1 obtained from numerical calculations.	44
Figure 5.4: Percent irrecoverable strain vs exponential for different rocks.....	45
Figure 5.5 Conceptual model to explain Poisson's ratio and Young's modulus as a function of sample damage.	45

Table of Table

Table 4.1: Pretest Berea sample measurements.....	17
Table 4.2: Castlegate sample dimensions and weight.	25
Table 4.3: Austin Chalk sample measurements.....	32
Table 4.4: Dundee sample measurements.....	38
Table 6.1 Berea measured data on loading stress path for 2000 psi confining stress.....	48
Table 6.2 Berea data on unloading stress path for 2000 psi confining stress.....	48
Table 6.3 Berea data values on loading stress path for 3000 psi confining stress.....	49
Table 6.4 Berea Data on unloading stress path for 3000 psi confining stress.....	49
Table 6.5 Berea data on loading stress path for 4000 psi confining stress.....	50
Table 6.6 Berea data on unloading stress path for 4000 psi confining stress.....	50
Table 6.7: Summary table for M1 and M2 as a function of stress for Berea.....	51
Table 6.8: Percent irrecoverable strain at each confining pressure.	51
Table 6.9 Castlegate data for 6500 psi confining on loading stress path.....	52
Table 6.10 Castlegate data for 6500 psi confining on unloading stress path.....	52
Table 6.11 Castlegate data for 5500 psi confining on loading stress path.....	52
Table 6.12 Castlegate data for 5500 psi confining on unloading stress path.....	53
Table 6.13 Castlegate data for 5000 psi confining on loading stress path.....	53
Table 6.14 Castlegate data for 5000 psi confining on unloading stress path.....	54
Table 6.15 Castlegate data for 4500 psi confining on loading stress path.....	54
Table 6.16 Castlegate data for 4500 psi confining on unloading stress path.....	55
Table 6.17 Castlegate data for 4000 psi confining on loading stress path.....	55
Table 6.18 Castlegate data for 4000 psi confining on unloading stress path.....	56
Table 6.19 Castlegate data for 3000 psi confining on both loading and unloading stress path (velocity data was not acquired).....	56
Table 6.20 Castlegate data for 2000 psi confining on both loading and unloading stress path (velocity data was not acquired).....	56
Table 6.21 Castlegate data for 1000 psi confining on both loading and unloading stress path (velocity data was not acquired).....	57
Table 6.22: Summary table for Castlegate on loading stress path. For 1000, 2000 & 3000 psi confining the velocity data could not be acquired due to equipment failure.....	57
Table 6.23 Austin Chalk static and dynamic data, 6500 psi, confining pressure on loading stress path.....	58
Table 6.24 Austin Chalk static and dynamic data at 6500 psi confining pressure on unloading stress path.....	58
Table 6.25 Austin Chalk static and dynamic data at 5000 psi confining pressure on loading stress path.....	58

Table 6.26 Austin Chalk static and dynamic data at 5000 psi confining pressure on unloading stress path.....	59
Table 6.27 Austin Chalk static and dynamic data at 3500 psi confining pressure on loading stress path.....	59
Table 6.28 Austin Chalk static and dynamic data at 3500 psi confining pressure on unloading stress path.....	59
Table 6.29 Austin Chalk static and dynamic data at 2000 psi confining pressure on loading stress path.....	60
Table 6.30 Austin Chalk static and dynamic data at 2000 psi confining pressure on unloading stress path.....	60
Table 6.31: Summary values for Austin Chalk on loading stress path obtained from quadratic fits.....	60
Table 6.32: Percent irrecoverable strain at each confining pressure.	60
Table 6.33 Dundee static and dynamic data at 1000 psi confining on loading stress path	61
Table 6.34 Dundee static and dynamic data at 1000 psi confining on unloading stress path	61
Table 6.35 Dundee static and dynamic data at 500 psi confining on loading stress path.	61
Table 6.36 Dundee static and dynamic data at 500 psi confining on unloading stress path	62
Table 6.37: Summary table for Dundee on loading stress path	62
Table 6.38: Percent irrecoverable strain at each confining pressure.	62

Chapter 1: Introduction

Static to dynamic correlations are locally dependent on mineralogy, texture and stress history. For example, in unconventional reservoirs they depend on the total organic content, thermal maturity, porosity and clay content. Similar complexity is seen for conventional reservoirs. Load bearing clays will increase irrecoverable strain and slow the acoustic velocity. Non-load bearing clays increase the velocity but do not affect the stress strain response. Small amounts of cements can significantly impact both static and dynamic data, depending on its distribution. The complexity of the rocks mineralogy and the dependency of these properties on the distribution of the minerals is the reason that only local correlations between static and dynamic properties have been developed.

The static and dynamic data for these correlations are typically obtained in the laboratory by measuring velocity while performing large strain compression measurements. We deviate significantly from typical measurement protocols by using “multistage” triaxial testing. This eliminates the “twinning” problem which significantly impacts the lack of repeatability inherent in single stage triaxial tests.

On a well scale the input data for prediction of static properties is often obtained from logs. The usual upscaling issues associated are therefore present if core data is used for the calibration. This emphasizes the need for models calibrated in terms of the actual mechanisms and the geology that determines their magnitude. It is this level of understanding which allows this upscaling to occur with confidence and provides the ability to extrapolate models outside their area of calibration. This upscaling allows the prediction of wellbore failure and sand control.

The next step is to map these properties on a field scale. If a model is successfully derived based on mineralogy, texture, and stress history the upscaling to a field scale is more likely to be successful. This makes possible the calibration of geomechanical and 4D seismic models.

The motivation behind this work is therefore to provide a more robust conversion between the Young's modulus and Poisson's ratio than that derived from empirically based correlations. It is expected this will involve the use of thin section and/or microCT data to provide a mineralogical and textural based model, allowing the upscaled wellbore and field models to be developed.

Chapter 2: Background

We now introduce the concepts of stress and strain, and Hooke's law. We define the point of positive dilatancy (PPD) and its connection with multistage triaxial tests. Also in this section we provide an elementary discussion of plasticity parameters: recoverable and irrecoverable strains, friction and dilatancy. All of these concepts are used in the data analysis section.

2.1 The Stress-Strain Curve

When an axial load is applied to a sample it will often initially exhibit linear elastic behavior. This region may be as small as 10^{-6} strain for a ductile rock to approximately one percent 10^{-1} for more lithified samples. The elastic strain is "recoverable" meaning that the sample will rebound this amount when unloaded. It involves compression of contacts, the elastic deformation of grains, and the opening and closing of compliant pores. With further axial strain, upon unloading, the measured

stress-strain path does not retrace the initial loading curve. The missing strain is called irrecoverable which is the measure of permanent sample deformation. The mechanisms include among others grain sliding, rotation, cracking, displacement, and permanent ductile grain deformation. With even further applied strain the sample often reaches the failure point, also known as the maximum compressive strength (MCS). At this point the sample unloads with further applied axial strain. Depending on a samples previous stress history, mineralogy and texture this point may never be reached, or require very high axial strains (>10%). The details of the post failure stress-strain curve depend on the mode of failure and the details of the sample makeup. The three regions are shown in Figure 2.1.

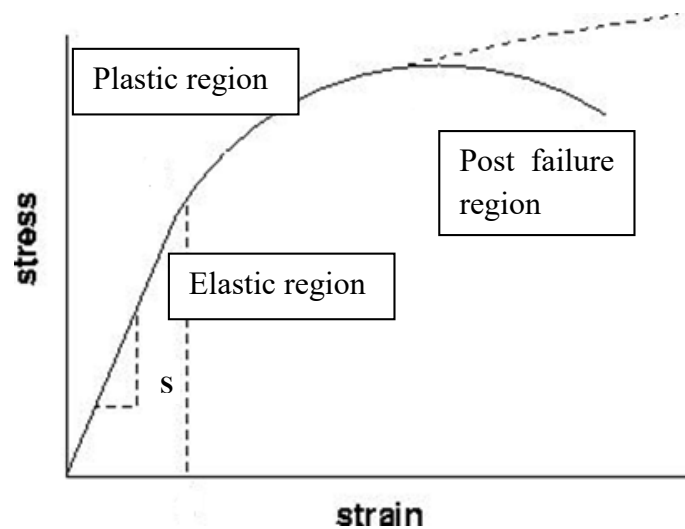


Figure 2.1: Typical stress-strain behavior of a rock under increasing axial stress. The three regions exhibited are defined by the magnitudes of the recoverable and irrecoverable strains. S is the slope of the stress strain curve and referred to as the sample stiffness. If the region is assumed to be elastic, the stiffness is equal to Young's modulus (E).

2.2 Deviatoric Stress

Deviatoric stress is defined as the difference between the axial stress and the radial stress. This stress is commonly associated with failure in rocks, in models such as Mohr-Coulomb, Drucker-Prager etc.

2.3 Strain and its Relation to the Point of Positive Dilatancy

A constant axial strain rate is the axial loading parameter used in all the measurements in this thesis. As the total axial strain increases for the test the sample also displaces in the radial direction. The ratio of the radial strain to the axial strain is a key material parameter called Poisson's ratio. The strain in rock samples is often expressed in millistrain. If L_o and r_o represent the original length and radius then the engineering axial strain is calculated by normalizing the total axial displacement to the sample's original length. This is given by,

$$\epsilon_a = \frac{\Delta L}{L_o}. \quad (2.1)$$

The engineering radial strain is given by,

$$\epsilon_r = \frac{\Delta r}{r_o}. \quad (2.2)$$

Engineering volumetric strain is defined as the change in volume divided by original volume

$$\epsilon_v = \frac{\Delta V}{V_o}. \quad (2.3)$$

The relation between volume strain, radial and axial strain for infinitesimal strains is shown by application of Hooke's law to be,

$$\epsilon_v = 2\epsilon_r + \epsilon_a. \quad (2.4)$$

By convention a smaller sample results from a positive strain while conversely a negative strain means that the sample is getting larger. Figure 2.2 shows deviatoric stress plotted against volumetric strain for a typical triaxial measurement. Initially the volumetric strain is positive (smaller sample), at even larger axial strains the volume strain goes negative. The point at which the volumetric strain changes sign is termed the point of positive dilatancy. We will use this point as the criteria to end the axial strain loading ramps in a multistage triaxial test.

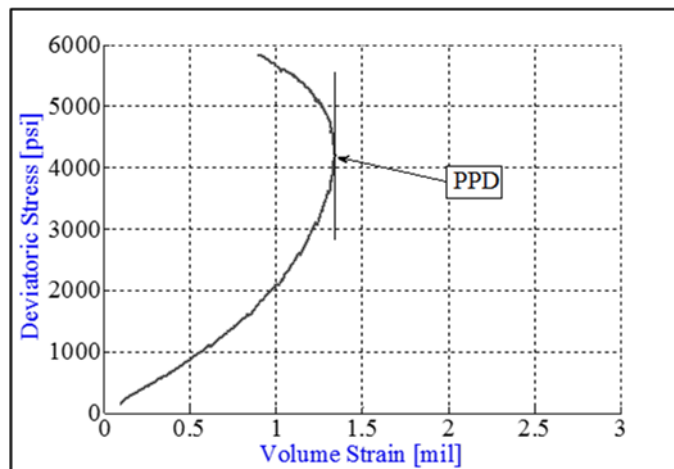


Figure 2.2: Deviatoric stress versus volumetric strain showing the point of positive dilatancy (PPD) where volumetric strain changes from increasing to decreasing. The tangent to the curve is vertical.

2.2 Modulus

We need the relationships between the various measures of sample stiffness, they are defined below.

- **Bulk modulus, K** , is the ratio of isostatic stress to volumetric strain under an isostatic stress path.
- **Shear modulus, μ** , is the ratio of shear stress to shear strain.
- **P wave modulus, $M = \rho V_p^2$** , is the ratio of axial stress to axial strain for a plane wave, or uniaxial-strain path.
- **Young's modulus, E** , is the ratio of axial stress to axial strain for a constant radial stress boundary condition. Young's modulus is calculated using Hooke's law from the compressional and shear velocity as follows:

$$E = \frac{3 * \left(\frac{V_p}{V_s}\right)^2 - 4}{\left(\frac{V_p}{V_s}\right)^2 - 1} * V_s^2 * \rho. \quad (2.5)$$

Where V_p and V_s are the compressional and shear wave velocity and ρ is the bulk density.

- **Poisson's ratio** is defined as the negative ratio of radial to axial strain, for a constant radial stress boundary condition.

$$\nu = - \frac{\varepsilon_r}{\varepsilon_a}. \quad (2.6)$$

Chapter 3 Experimental Equipment and Data Analysis

3.1 Lab Equipment

The standard two inch long and one inch diameter right cylindrical sample was used in all the experiments. The sample is mounted using a Viton sleeve between two end caps as shown in Figure 3.1. Two LVDT's are used to measure the axial strain between the endcaps. A cantilever bridge is used to perform a two point measurement of the radial strain. It consists of two flexible arms with strain gauges mounted on opposite sides in a Wheatstone bridge arrangement. Flexing the arms unbalances the bridge. The average of the two radial or axial measurements represents the final data. The endcaps have piezoelectric transducers which are used in a "pitch and catch" arrangement to acquire axial shear and compressional acoustic data at one MHz.

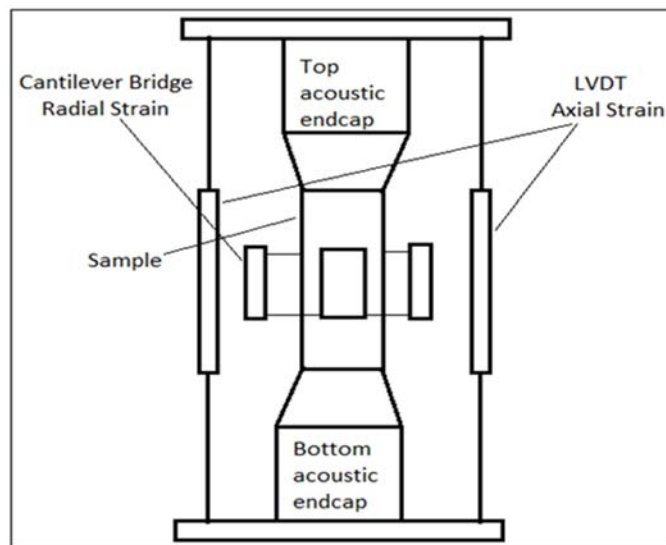


Figure 3.1: The sample mounting and measurement assembly with LVDTs and cantilever bridge and acoustic endcaps. The average of the axial and radial measurements is used.

The assembly shown in figure 3.1 is placed inside the cylindrical pressure vessel shown in figure 3.2. The pressure vessel is filled with confining fluid (mineral oil) to apply the radial stress.



Figure 3.2: The cylindrical pressure vessel in which the sample assembly is placed. The maximum pressure is 12000 psi which is applied by displacement pumps under PID (proportional integral differential) control.

The internal load cell is located on the bottom of the vessel and is used to measure the axial load. This load is applied through a 1 1/2 inch diameter piston using a ball screw press. Figure 3.3 is a picture of the experimental setup.



Figure 3.3: Experimental setup including the computerized control panel. The entire apparatus is PID controlled and capable of 75000 lb. axial load and 12000 psi confining stress.

3.2 Triaxial Tests

By definition a standard triaxial test is performed at a constant confining pressure. The loading parameter is usually a constant axial strain rate. Brittle samples at failure will have dramatic results if the equipment is controlling on axial load. As the axial strain increases the deviatoric stress will increase until the sample reaches its maximum compressive strength (MCS). Figure 3.4 shows typical triaxial stress-strain data. The purple line shows a constant confining pressure of 1000 psi. There are also unload and reload cycles of the deviatoric stress to measure irrecoverable strains and the unloading and reloading Young's modulus and Poisson's ratio.

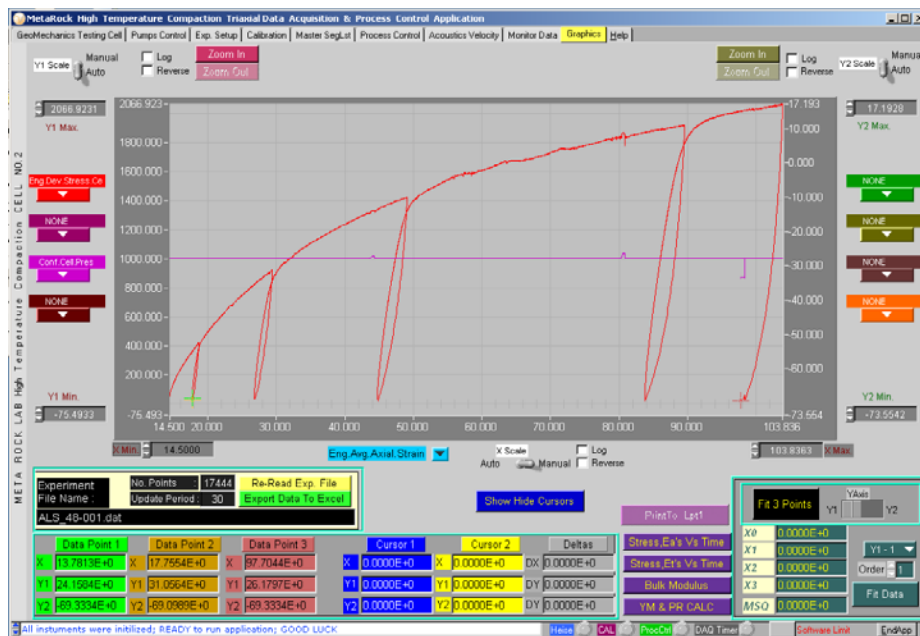


Figure 3.4: Data for a typical triaxial test. The deviatoric stress is plotted on the vertical axis. Axial strain is plotted on the horizontal axis. This is a conventional triaxial test where the confining stress is held constant throughout.

3.3 Multistage Triaxial test

A multistage triaxial (MST) test is similar to a conventional triaxial test except that it has multiple stages of confining pressure. Instead of raising the deviatoric stress to

the maximum compressive strength (MCS) at constant confining stress, the loading cycle is stopped at the point of positive dilatancy (PPD). The sample is then unloaded to a low deviatoric stress, the confining pressure is raised and the cycle is repeated at the new confining stress. All the experiments were performed at a constant axial strain rate of five microstrains per second. Figure 3.5 shows one cycle of a MST, the red curve is at a lower confining stress than the blue curve. The PPD is that point where the slope of the deviatoric stress versus volumetric strain becomes vertical as shown in Figure 2.2. The methodology used to perform a multi-stage test is suggested by Al-Salman, Myers and Sharf-Aldin. (2015).

Earlier techniques have used different unloading points to perform a MST. The unloading point used in the ISRM standard (Kovari, Tisa 1975) is when the axial stress-strain curve becomes horizontal i.e. its slope is zero. This is at a higher stress than used here. This is the maximum compressive strength but for brittle samples it is problematic to stop the axial ramp before sample failure (unloading). A different unloading point is used by Taheri, Tani (2008), they recommend using the maximum value for Young's modulus (E (secant) = max). This point is at a lower stress than used here. There would be a larger correction factor to estimate the compressive strength than using the PPD. To our knowledge this correction factor has not yet been developed.

The PPD has been chosen instead of these unloading points, it represents a compromise between them. Using this point the sample damage appears to be minimal and the data is easily corrected (Al-Salman, Myers, Sharf-Aldin, 2015). This point also can be chosen by different operators with good repeatability.

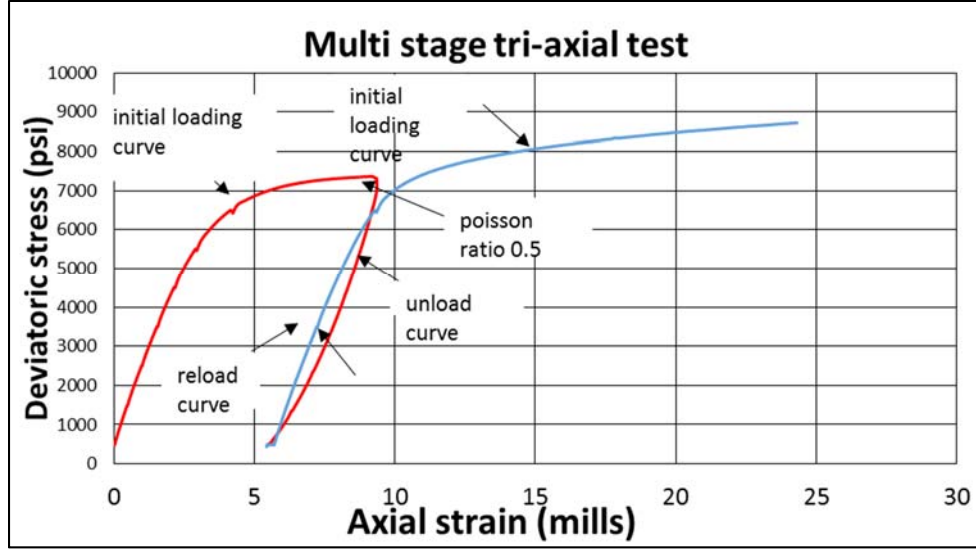


Figure 3.5: Stress path for multistage triaxial test showing deviatoric stress on y-axis and axial strain on x-axis. The red curve is taken at a lower confining pressure than the blue curve. The sample is unloaded at the point of positive dilatancy.

An alternative method to that discussed above for picking the PPD involves monitoring a real time calculation of Poisson's ratio. An infinite slope means that the increment of volumetric strain with increasing axial strain will be zero:

$$d\epsilon_v = 0. \quad (3.1)$$

Applying equation 2.4

$$d\epsilon_v = 2d\epsilon_r + d\epsilon_a = 0 \rightarrow \frac{d\epsilon_r}{d\epsilon_a} = -0.5 \text{ and} \quad (3.2)$$

$$v = -1/2. \quad (3.3)$$

At the PPD the Poisson's ratio is one half. This is easily chosen from a real time calculation of Poisson's ratio and was the technique used to pick the beginning of the unloading reloading cycle.

3.4 Experimental Error

The experimental error in calculating Young's modulus from the static data is approximately two percent based on calibration to aluminum standards. The error in the dynamic data is approximately one percent for compressional velocities and three percent for shear velocities. These were also based on measurements on aluminum and lucite standards.

3.5 Dynamic Data

The dynamic data was obtained at intervals of 1000 psi deviatoric stress. This was done throughout the initial loading curve and the subsequent unloading and reloading cycles.

Initially the bulk modulus and shear modulus were calculated from the static data and compared to the dynamic data. The static data was not equal to the dynamic data at the start of the unloading or reloading cycles. A simple physical argument requires this to be true i.e. it should not matter how the modulus is measured. It was therefore concluded that the static data cannot be converted from one stress path to another. The reason for this is that linear elastic theory was used to convert the static data. The static data is not linear and the samples may be anisotropic, so this conversion is inappropriate (Hooke's law does not hold). We therefore converted the small strain acoustic data from the shear and plane wave modulus to Young's modulus and Poisson's ratio for comparison.

3.6 Quadratic Fits to the Static Data

We now make the assumption that the axial stress may be expanded in terms of the axial strain in a Taylor series about the zero strain value. We will examine the usefulness of this assumption in the next section. Keeping only up to the quadratic term we arrive at Eq. 3.4:

$$\sigma = M_2\varepsilon^2 + M_1\varepsilon + \sigma_0. \quad (3.4)$$

For small strains ($\varepsilon \rightarrow 0$ $M_2\varepsilon^2 \ll M_1\varepsilon$) this reduces to the conventional Hooke's law approach. Equation 3.4 therefore implies that M_1 is equal to Young's modulus at small strains. As discussed above it also must be identical for both static and dynamic data. Equation 3.4 also allows the separation of the stress versus strain data into linear elastic (M_1) and nonlinear elastic (M_2) terms. We limit ourselves to a second order term which will be used to fit the majority of the reloading data.

M_2 is coined the "Hypermodulus" which represents the nonlinear elastic contribution to the unloading and reloading curves. M_2 correlates with sample damage which will be discussed below. A typical fit of equation 3.4 to sample data is shown in Figure 3.6. They agree to within the size of the data points.

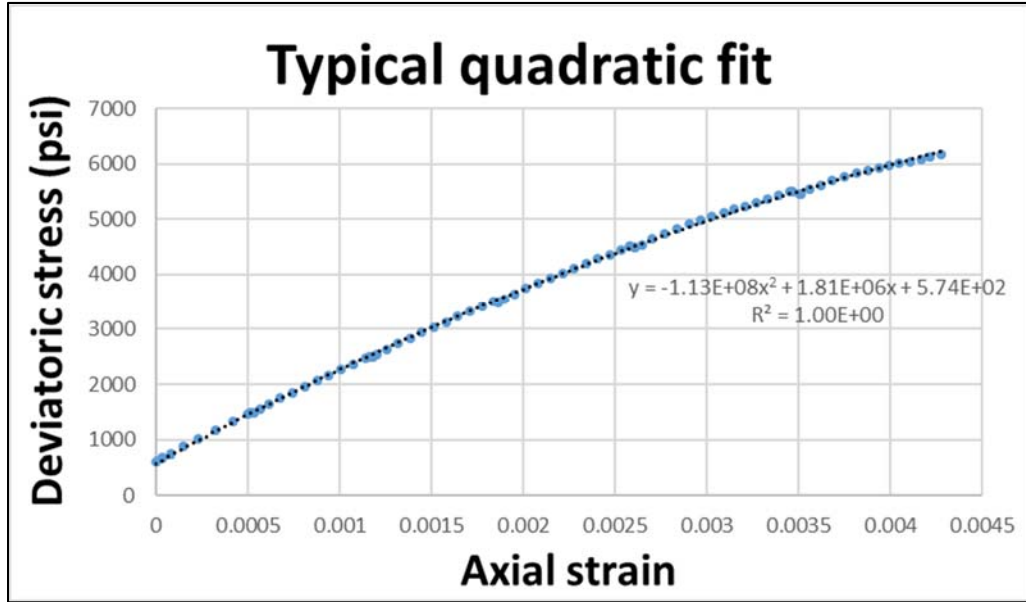


Figure 3.6: A typical quadratic fit for deviatoric stress versus strain for Austin Chalk at 5000 psi confining stress on the loading stress path. This fit is within the expected error.

We will first determine the values of M_1 and M_2 by a numerical calculation of the derivatives on the unloading and reloading cycles. M_1 and M_2 are calculated from both a quadratic fit and numerically to check the quality and consistency of the data.

We are not using the initial two percent of the unloading and reloading cycles to perform the quadratic fits. This portion of the curve is dominated by equipment hysteresis and possible effects due to sample creep. On the reloading curve the data is limited to avoid the portion of the curve that involves additional sample damage. We have therefore performed quadratic fits to successively larger percentages of the total data on the reloading curve. The values for M_1 and M_2 are shown in Figure 3.7. M_1 is relatively insensitive to the range of data. M_2 however does show a dependence as the axial stress approaches the values obtained on the previous reloading cycle. When the lower deviatoric stress data is used in the fits the value of M_2 is relatively stable. In this case at

shown in Figure 3.7 at 3/4 the total range of the data value starts to change at low stresses. When fitting for M_2 , we therefore only include data through the first half of the reloading cycle. We believe this is an important diagnostic when sample damage starts to occur on the reloading cycle. We will validate this through thin section and microCT examination of the samples.

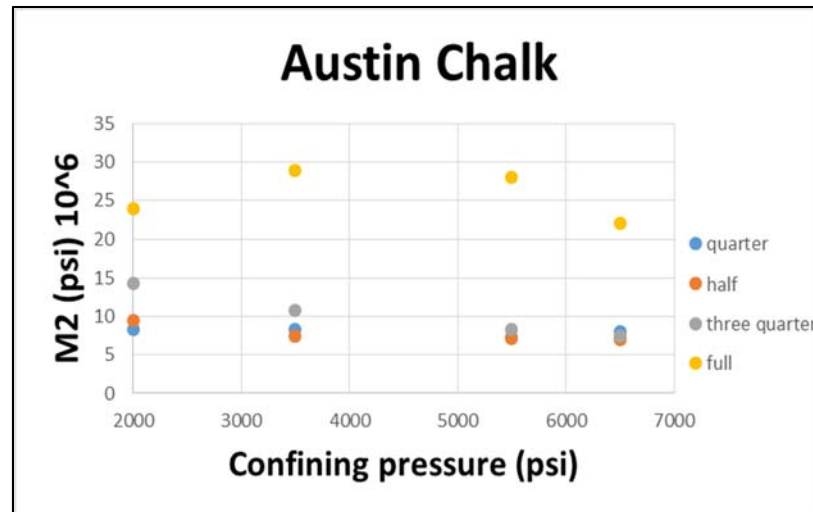
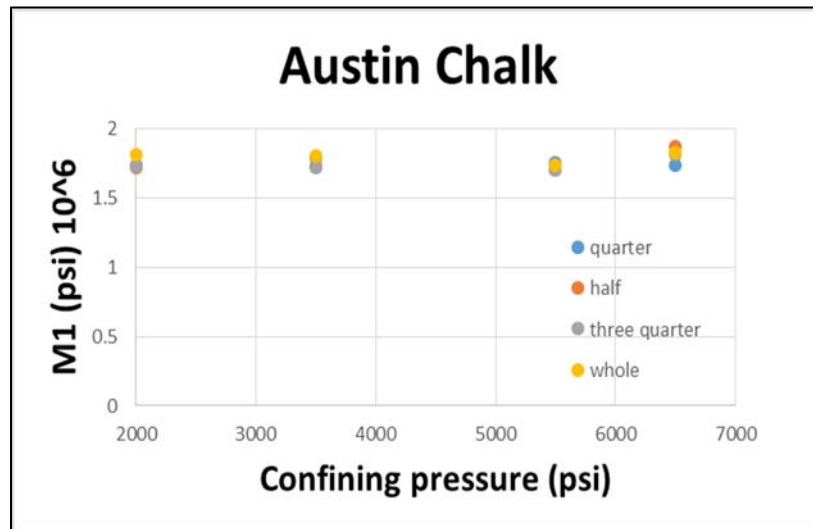


Figure 3.7: M_1 and M_2 values obtained by fitting portions of the reloading curve. As the percentage of the curve is increased, M_1 is constant but M_2 is constant only when one quarter or one half of the reloading curve is fit. The value of M_2 is determined from the portion of the curve where the value is stable.

3.7 Measurement of Irrecoverable Strains

Figure 3.8 shows a plot of confining stress versus axial strain for a multistage triaxial test. Irrecoverable strain is defined as the strain that is not recovered by unloading the sample after reaching the point of positive dilatancy.

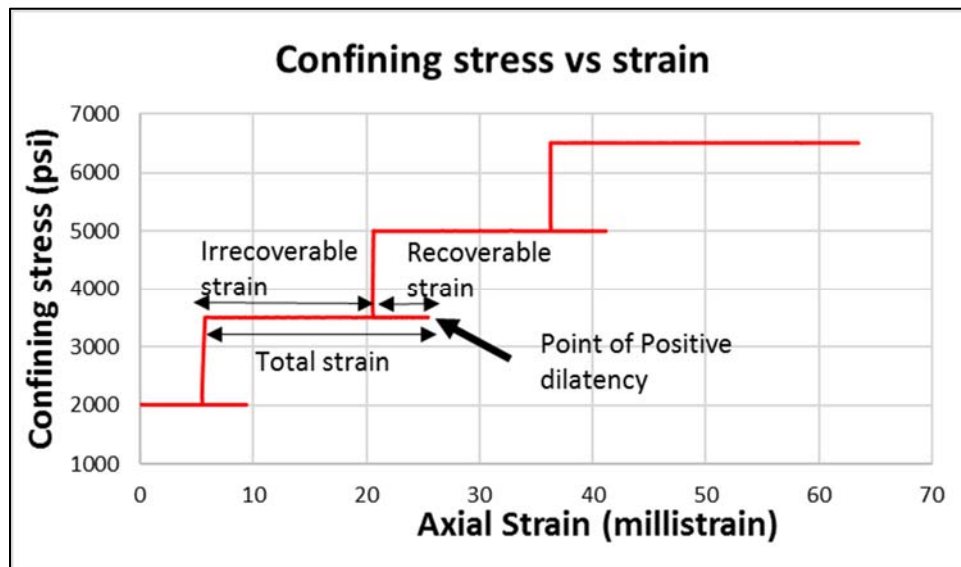


Figure 3.8: Confining stress versus strain for the MST test for Austin Chalk. Each horizontal line is a cycle of the loading and unloading of the sample. The vertical lines are due to the increase of 1500 psi in the confining stress. The percent irrecoverable stain is the irrecoverable strain normalized to the total strain at each confining stress.

Figure 3.8 shows the recoverable and irrecoverable strain clearly delineated. The percent irrecoverable stain is the irrecoverable strain normalized to the total strain. It is calculated at each confining stress for each sample. It represents the total irrecoverable strain, since the sample is unloaded to a common low deviatoric stress. It is observed to be relatively independent of confining stress. This is attributed to the competition between the increasing confining stress, which tends to close cracks and the increasing

deviatoric stress which initiates and lengthens cracks. Therefore an average value has been used as representative for each sample.

Chapter 4 Data Analysis

4.1 Berea Sandstone

Berea sandstone is named after Berea, Cuyahoga County, where it is extracted to use as a grindstone. It is a very fine grained rock with grains being angular rather than rounded. The grains are predominantly composed of quartz held together by silica cements. (Andrews 1870) Figure 4.1 shows the post and pretest pictures of the sample tested.

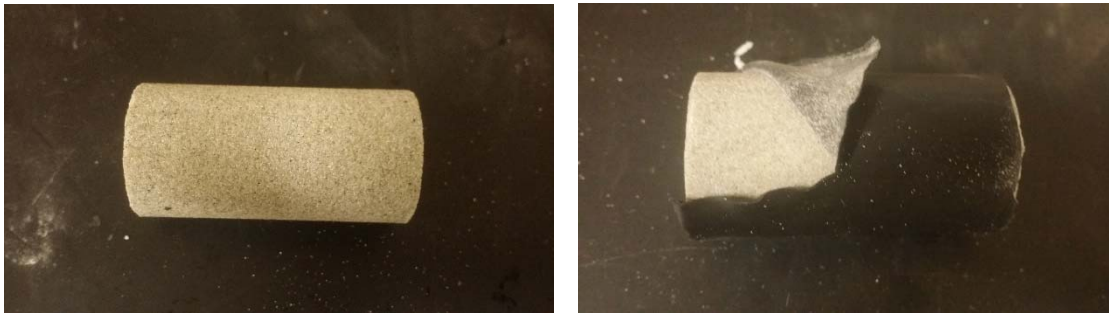


Figure 4.1: The pretest and post test sample pictures. The sample is stored in a Viton sleeve post test to keep it intact. This sample exhibited a brittle failure.

Table 4.1: Pretest Berea sample measurements

Length	2.042 in
Diameter	1.014 in
Weight	59.65 g
Bulk density	2.20 g/cc

For Berea the multistage triaxial test was performed at confining pressures of 100, 1000, 2000, 3000 and 4000 psi. Figure 4.2 is the “fountain plot” for this MST test. A fountain plot contains axial, radial and volumetric strain plotted simultaneously. As shown the radial strains are negative because the sample diameter is increasing.

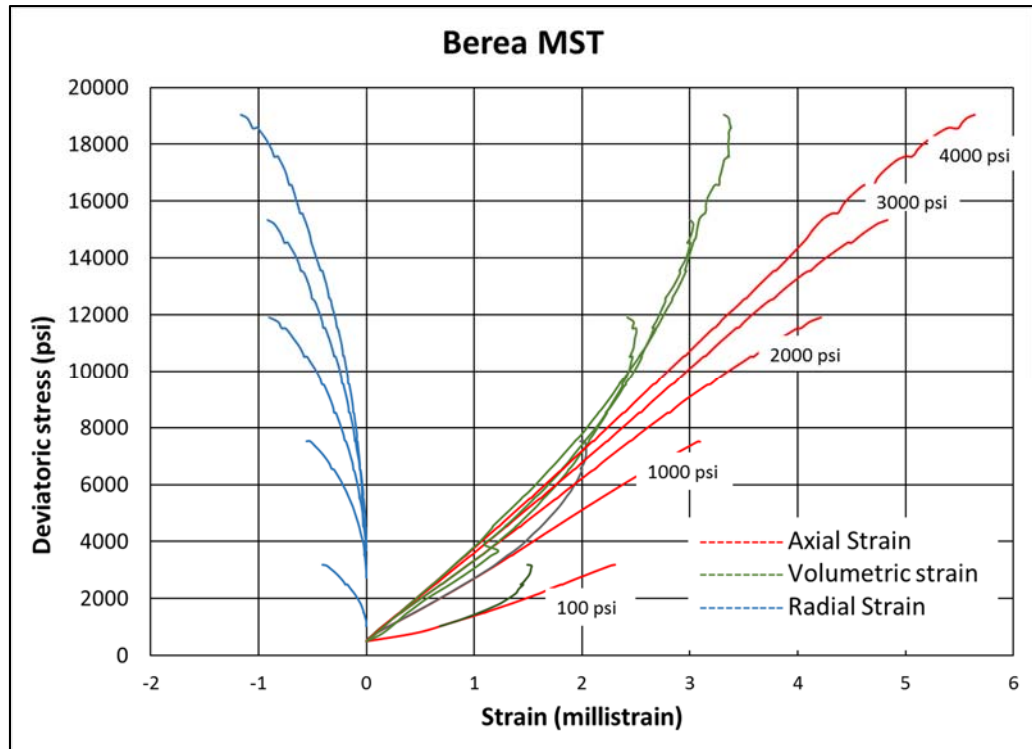


Figure 4.2: Multistage triaxial test results for Berea showing axial, radial and volumetric strains as function of deviatoric stress. The strains are zeroed at each confining pressure. The slight dips in the data are due to creep effects that occur when the axial loading is halted for the velocity measurement.

In Figure 4.2 there is a significant effect of confining pressure on the slope of axial stress versus strain data. The stiffness increases with increasing confining pressure and is interpreted as due to the closing of compliant pores.

In order to compare our results with earlier published MST work (Al-Salman, Myers, Sharf-Aldin, 2015) we have run conventional triaxial tests on Berea to measure

the correction factor for the MST. The deviatoric stress is ramped to the maximum compressive stress (failure) in individual triaxial tests. Figure 4.3 shows the single stage triaxial fountain plot for Berea.

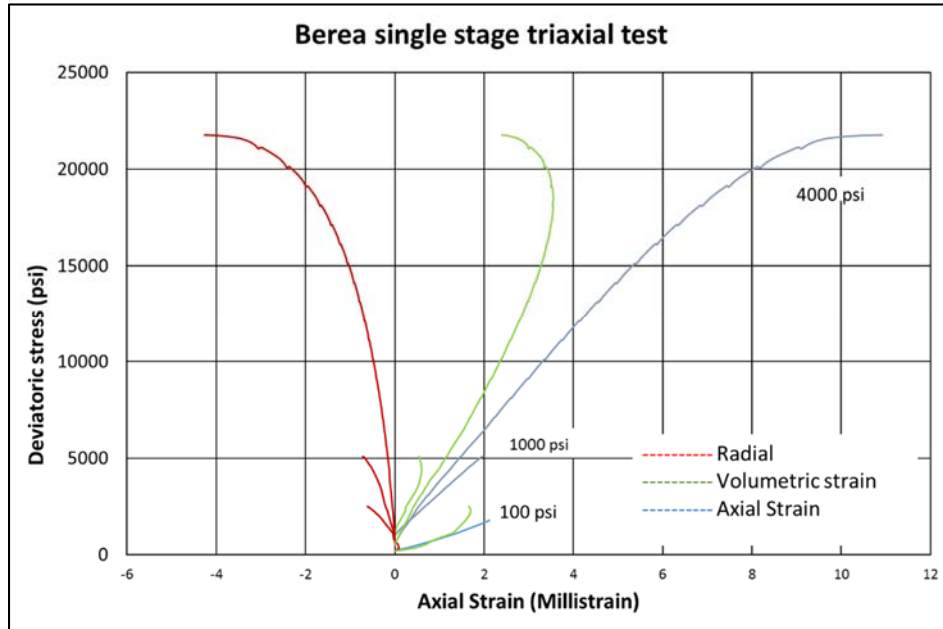


Figure 4.3: The single stage triaxial tests for Berea showing the axial, radial and volumetric strains as function of deviatoric stress. Each of these tests was run on a separate sample. The effects of sample twinning are also evident when compared to Figure 4.2

4.1.1 Comparison of Static and Dynamic Young's Modulus

Figure 4.4 shows the plot of static and dynamic Young's Modulus versus strain for loading and unloading data at different confining pressures. Due to equipment issues, we could not obtain the dynamic data the lowest confining stress for 1000 psi. The dynamic data was taken at increments of 1000 psi deviatoric stress along the entire ramp. The static Young's modulus is the derivative of the static curve at this same stress, which was calculated over a range of 1/10 millistrain. As shown in the Figure 4.4 the static and dynamic data is equal at low axial strain. A similar result was reported by Fjaer et al (2015).

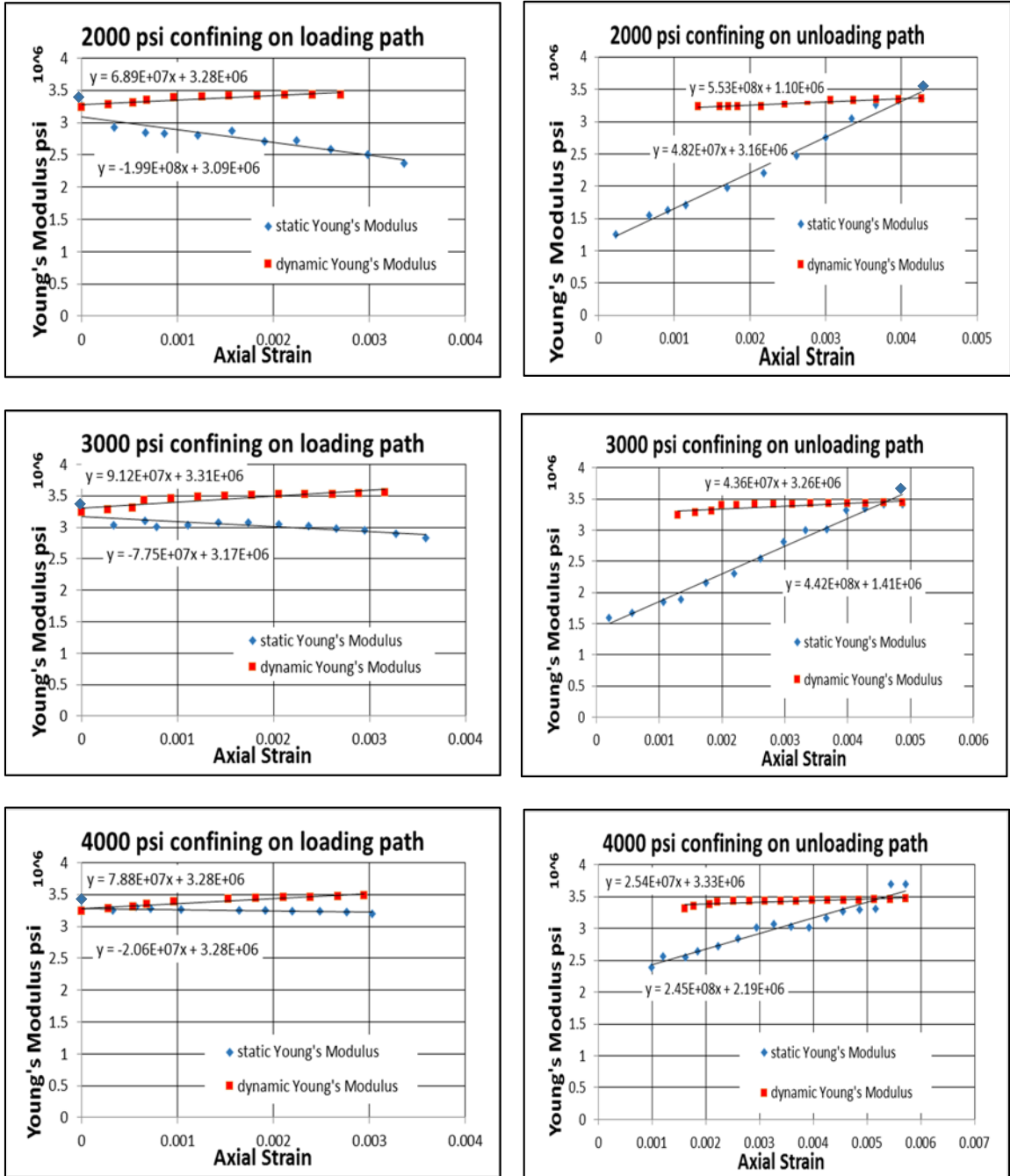


Figure 4.4: Static and dynamic YM versus strain on loading and unloading stress path respectively for different confining pressure. Static and dynamic Young's modulus (M_1) are equal at low strain.

The static and dynamic data in Figure 4.4 have different trends with increasing axial strain. For the static data, Young's modulus is decreasing while for dynamic data it increases. For dynamic data the contact modulus plays the dominant role. With increasing deviatoric stress the contact area between grains increases and therefore the dynamic modulus increases, consistent with a Hertzian contact model (Hertz, 1896). For static measurements the dominant mechanism is interpreted as the opening of compliant pores on the reloading cycle and their closing on the unloading cycle. These pores will become more compliant as they are opened.

This conceptual model is consistent with the observation that the differences between the static and dynamic moduli decreases with increasing confining stress. This effect was largest for Berea and is related to the large confining stress dependence of the stiffness in the individual triaxial ramps. Detailed models will be reported in future work.

4.1.2 Berea small strain modulus (M_1)

We have used two different methods to compute M_1 for the static data. The first method discussed above is by numerically calculating the local derivative at the start of loading and unloading stress path. The second method is applying a quadratic fit to the stress-strain curve. For direct comparison at the different confining stresses we have zeroed the strain at the start of the loading stress path. On the unload stress path, the starting point is the PPD.

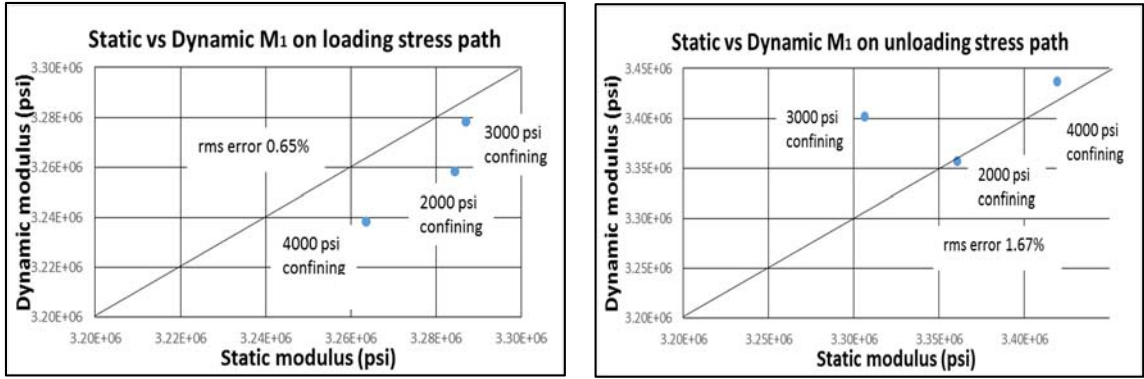


Figure 4.5a, b: Static vs Dynamic small strain modulus on loading and unloading stress path respectively showing they are both equal within experimental error.

As shown in figure 4.5 a and b near zero strain the static and dynamic Young's moduli are equal as determined by the two methods.

4.1.3 Berea Hypermodulus

M_2 is the second order term of the quadratic fit to the unloading and reloading axial stress-strain curve. Within a few percent M_2 as determined by a quadratic fit is equal to 1/2 the slope of Young's modulus versus axial strain plot (Figure 4.4). The data is in table 6.7 in the appendix. In figure 4.6 a, b M_2 (from quadratic fits) has been plotted against confining pressure for both loading and unloading stress path on a semilog plot.

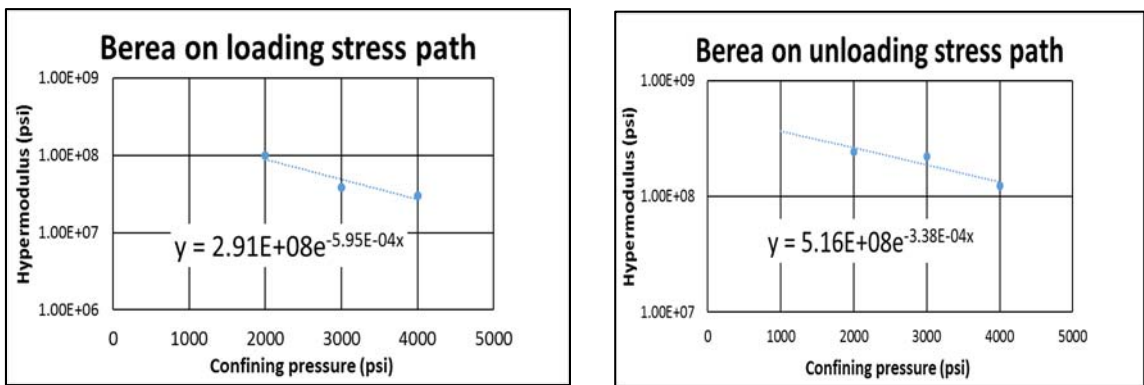


Figure 4.6 a, b: Hyper modulus versus confining pressure for both loading and unloading stress path. M_2 decreases with increasing confining pressure. This is due to the effect of cracks closing.

We can see that in both loading and unloading stress path hypermodulus (M2) decreases with increasing axial strain. The tabulated values are in appendix.

4.1.4 Berea Poisson's ratio

In Figures 4.7a and 4.7b, Poisson's ratio is plotted as a function of deviatoric stress for Berea on both loading and unloading stress paths.

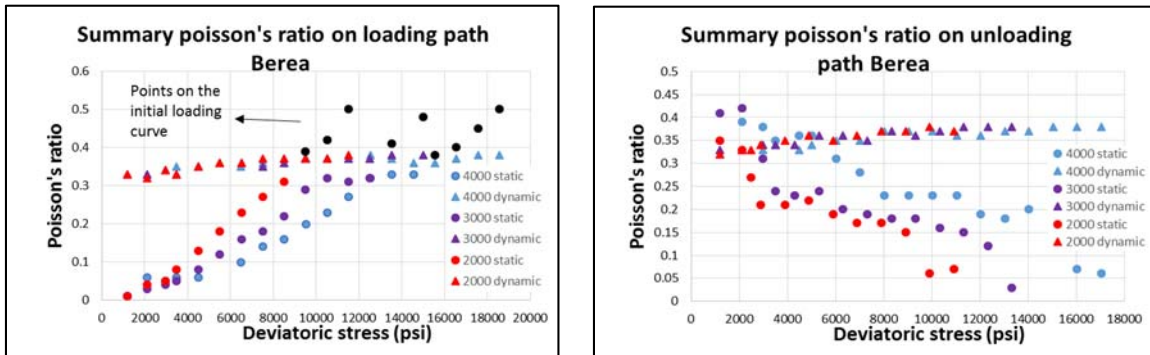


Figure 4.7 a, b: Berea Poisson's ratio on loading and unloading stress path respectively for different confining pressures. Poisson's ratio is near zero at the beginning of the cycles and approaches the dynamic value at the end. The points in black are interpreted to be on the initial loading curve.

At the start of either the unloading or reloading cycles the static Poisson's ratio is very low. In this case the loading and the radial displacement are in perpendicular direction. As either cycle progresses the radial strain increases and Poisson's ratio starts to increase and approaches the dynamic Poisson's ratio. At the beginning or the end of either cycle, the radial response is only due to the response of the grain contacts. The simple model is presented in section 5.3. The dynamic Poisson's ratio has smaller stress dependence consistent with the contact model.

4.1.5 Berea - Irrecoverable strain

We calculate recoverable and irrecoverable strain directly with the help of figure 4.8. The percent irrecoverable strain is calculated as explained in section 3.7. The value at each confining stress step has been tabulated in the appendix.

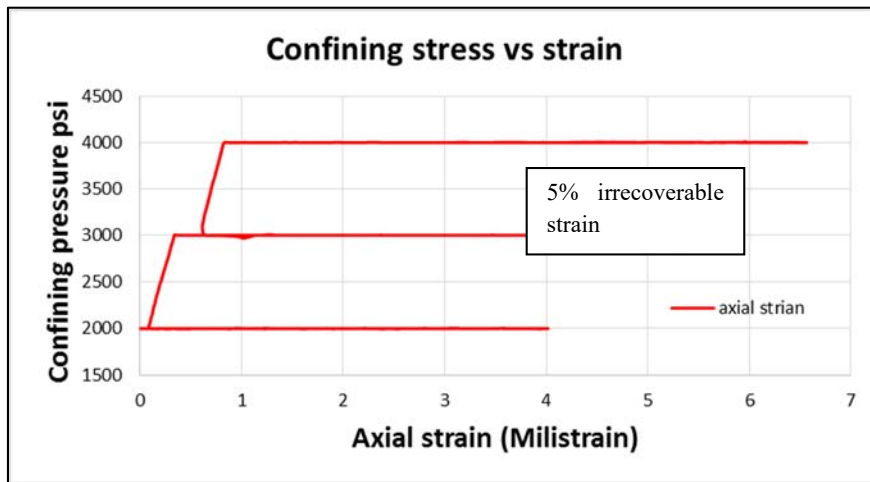


Figure 4.8: The Berea confining pressure versus axial strain. The average value of 5% was obtained. This was the lowest measured value of irrecoverable strain.

4.2 Castlegate

Castlegate is a sandstone from a Mesozoic geologic formation outcrop in Utah. For Castlegate the multistage test was performed on eight different confining pressures ranging from 1000 psi to 6500 psi. The pretest and posttest sample pictures are shown in Figure 4.9. Table 4.2 contains the sample measurements. Figure 4.10 is the fountain plot .



Figure 4.9: Castlegate post and pretest sample pictures. The posttest sample is kept in a Viton sleeve to keep it intact. This sample exhibited a brittle failure.

Table 4.2: Castlegate sample dimensions and weight.

Length	1.946 in
Diameter	1.023 in
Weight	49.38 g
Bulk density	1.88 g/cc

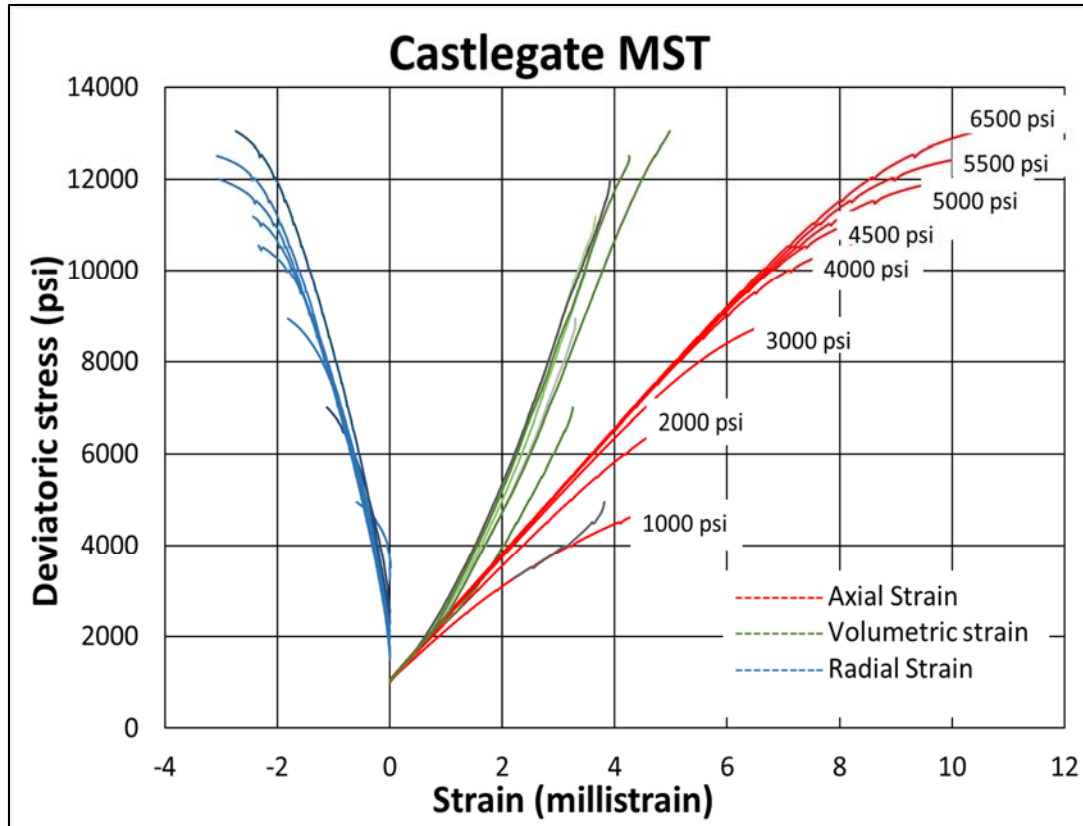


Figure 4.10: Fountain plot for Castlegate showing axial, confining and radial strains. At lower confining pressure the slope is sensitive to confining pressure but for higher confining pressures the slope is almost constant.

The Mohr-Coulomb plot for Castlegate is shown in Figure 4.11. The maximum compressive strength was obtained by multiplying the axial stress at the positive point of dilatancy by 1.2. The friction angle is 30.4 degrees the cohesion is 1192 psi. These numbers are both less than the values obtained for Berea. This sample had a more ductile failure than Berea. This is evident by the increased nonlinearity near the PPD.

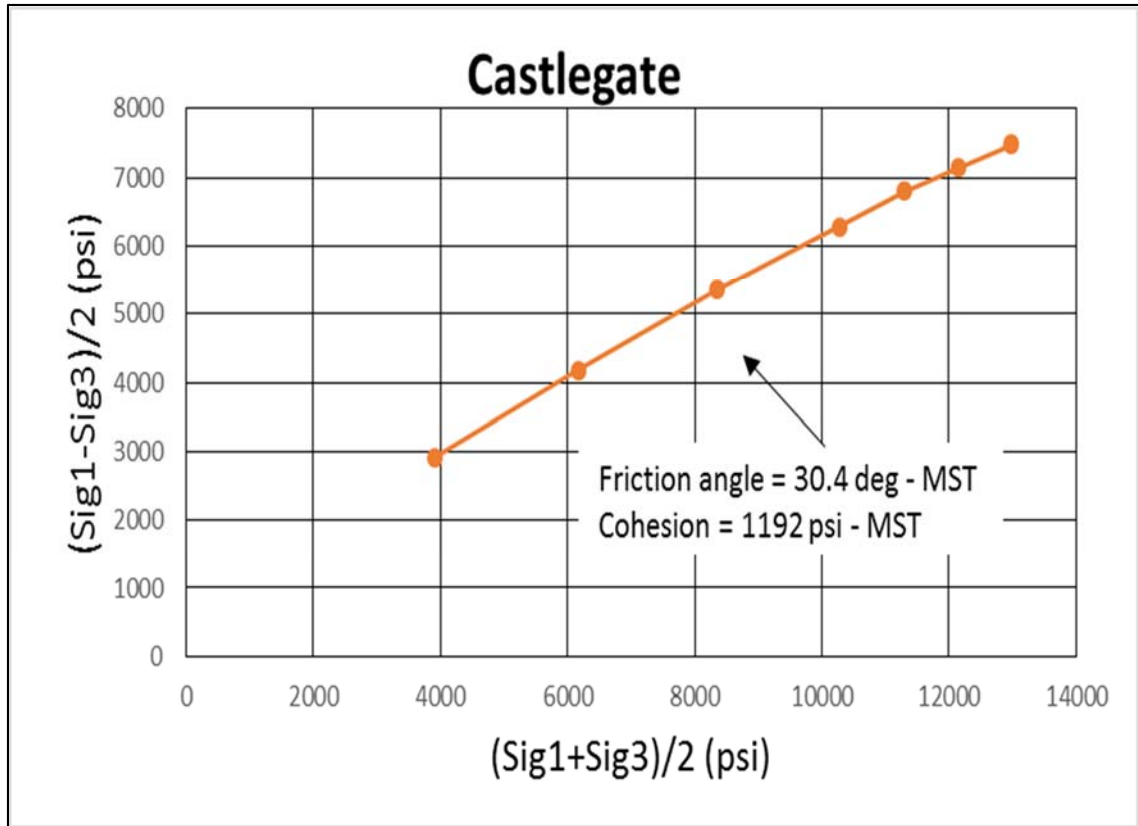


Figure 4.11: The p/q plot for multistage triaxial test for Castlegate showing friction angle of 30.4° and 1192 psi cohesion. Sig1 and Sig3 are axial and radial stress respectively.

4.2.1 Comparison of Static and Dynamic Young's Modulus

Figure 4.12 is the plot of Young's modulus versus axial strain at different confining pressures for both the loading and unloading stress paths for Castlegate. The data is qualitatively the same as Berea. The static and dynamic M_1 values are equal at the start of loading and unloading stress cycle. The difference between static and dynamic Young's modulus again increases with increasing stress on loading stress path and on the unloading stress path the difference decreases with increasing stress.

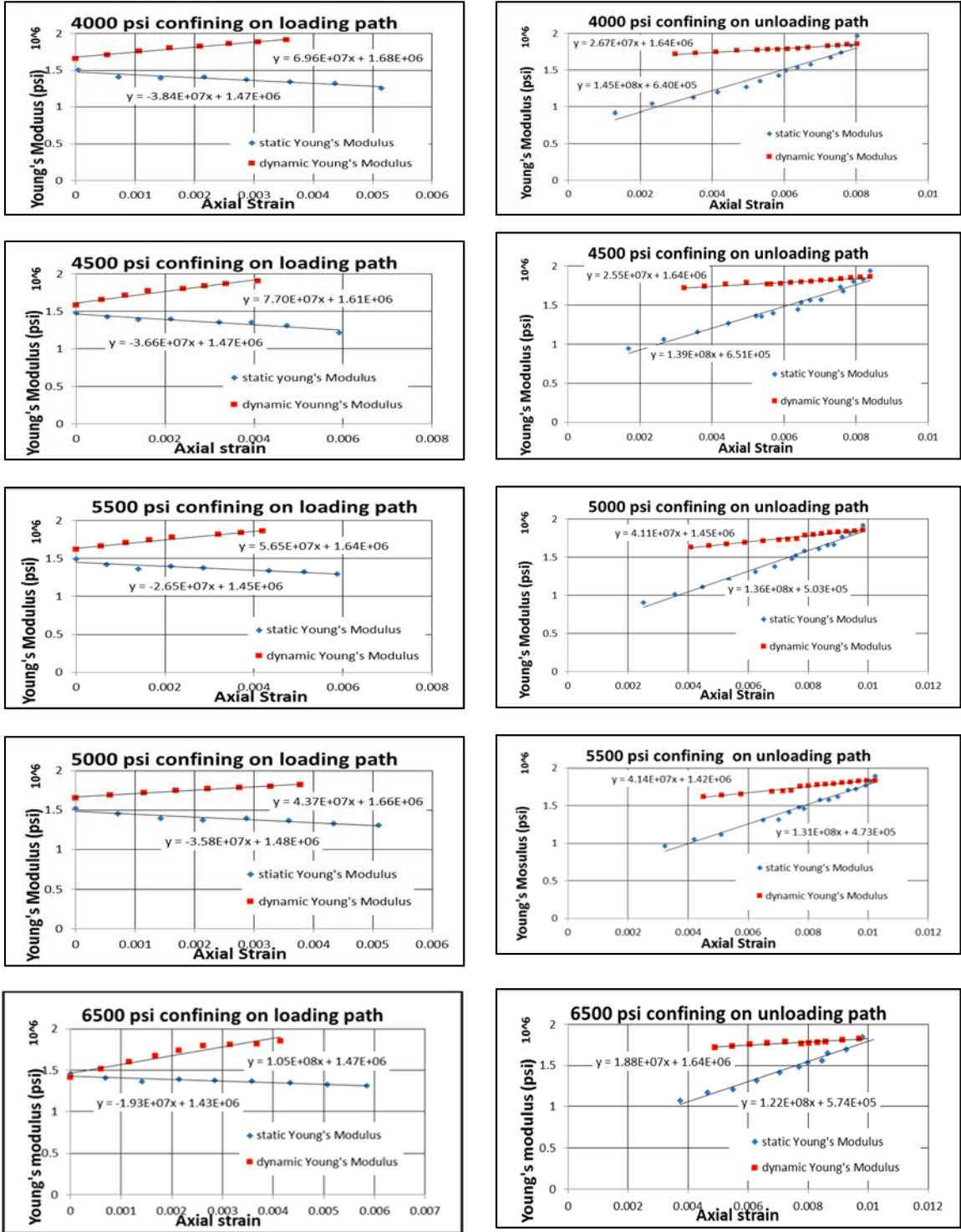


Figure 4.12: Static and dynamic Young's modulus versus strain on loading and unloading stress paths. Similar to Berea the static modulus decreases whereas dynamic modulus increases with increasing deviatoric stress. Very good agreement is obtained between the static and dynamic data at low strains.

For the remaining three confining pressures (3000, 2000, 1000 psi), no dynamic data was obtained due to equipment failure.

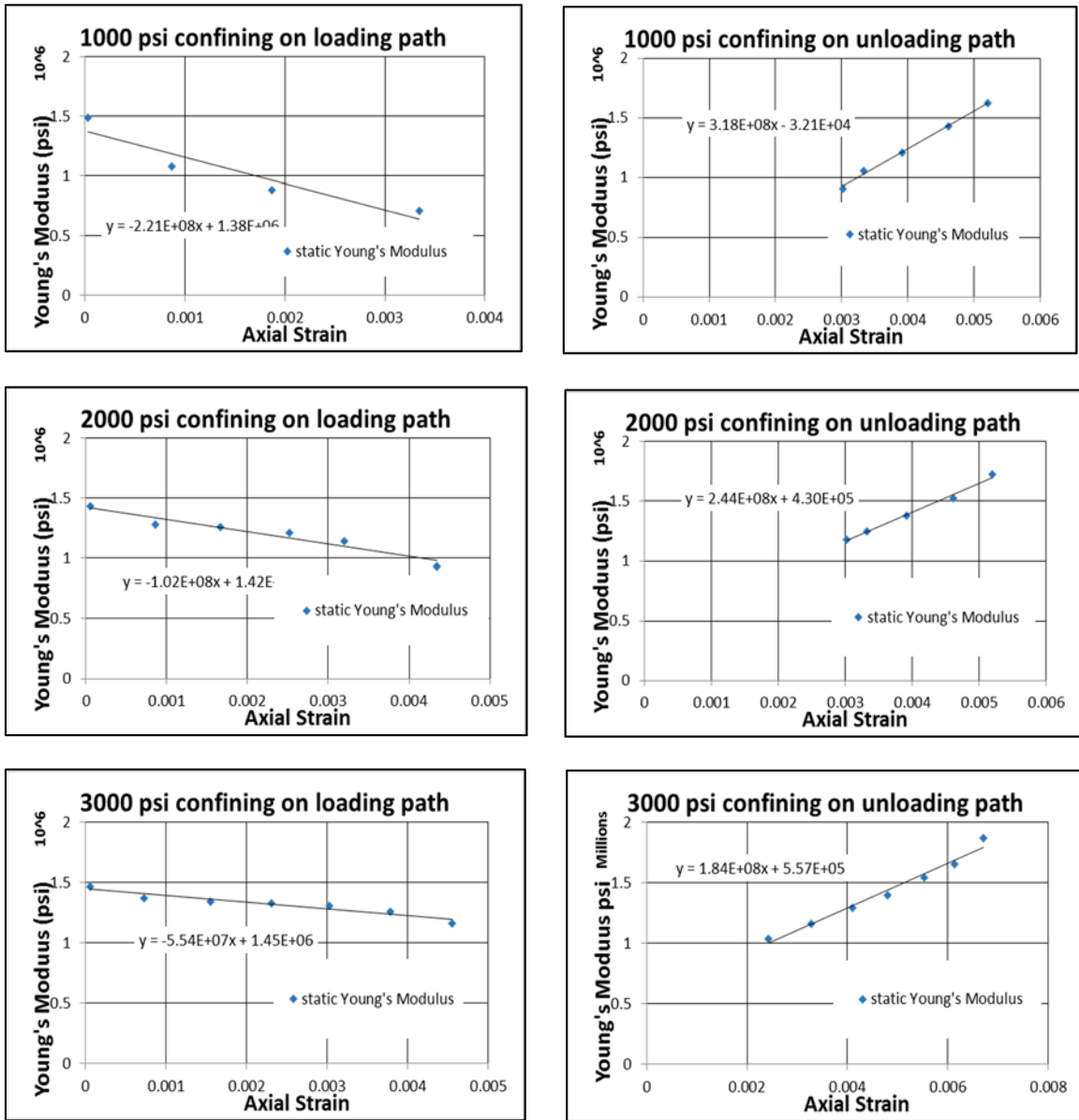


Figure 4.13 a, b: The Static data for 1000, 2000 and 3000 psi confining pressures on both loading and unloading stress path. We did not obtain dynamic data due to equipment failure.

4.2.2 Castlegate Young's modulus

Figures 4.14 a, b are the plots of static M_1 obtained from quadratic fits versus dynamic M_1 obtained from velocities. The RMS error is within the error discussed in section 3.4.

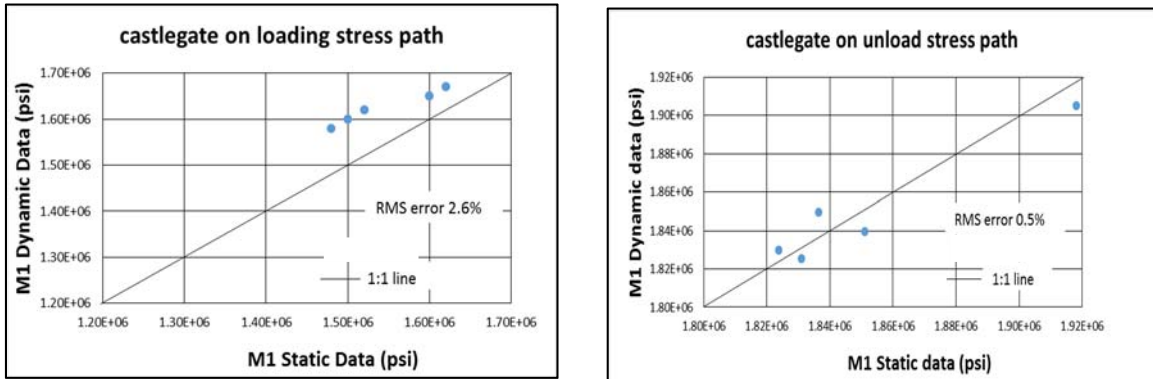


Figure 4.14 a, b: Static versus dynamic small strain modulus on the loading and unloading stress path. They are equal within experimental error. The values are tabulated in appendix.

4.2.3 Castlegate Hypermodulus

Figure 4.15a and Figure 4.15b are semilog plots of M_2 versus confining pressure. M_2 again decreases with increasing confining pressure. The tabulated M_1 and M_2 values are in appendix.

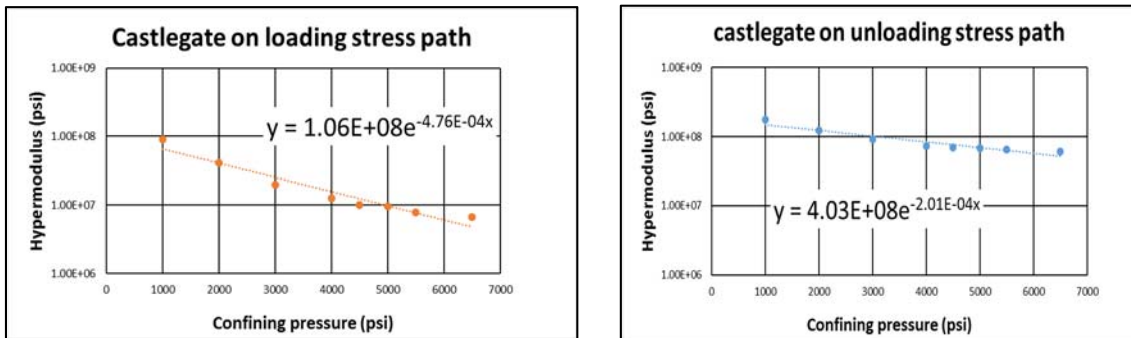


Figure 4.15 a, b: Hypermodulus versus confining pressure on both loading and unloading stress path. The value of M_2 (degree of nonlinearity of Young's modulus) decreases with increasing confining pressure.

4.2.4 Castlegate - Poisson's ratio

Figure 4.16 is the plot for Poisson's ratio versus deviatoric stress on the loading and unloading stress path. The dynamic Poisson's ratio, which is dominated by the contact modulus, is less stress dependent than the static Poisson's ratio. The static Poisson's ratio is again small at the start of the loading stress path.

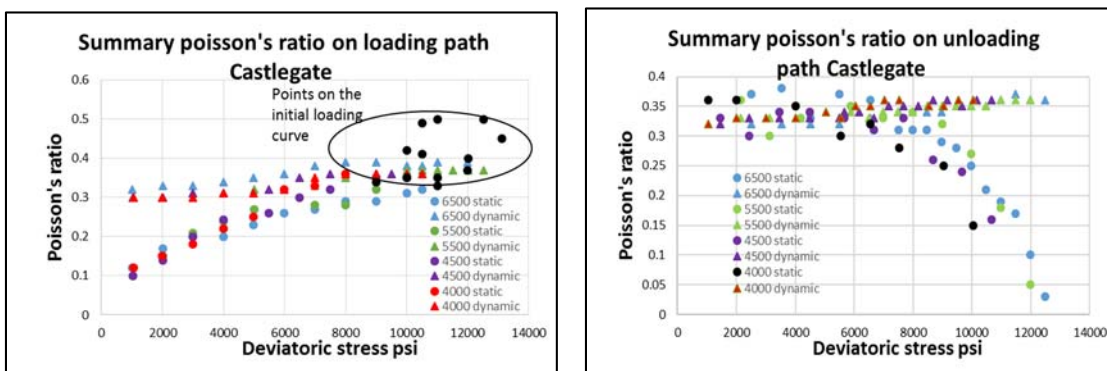


Figure 4.16 a, b: Castlegate Poisson's ratio on the loading and unloading stress path. Dynamic Poisson's ratio is constant whereas static is small at the beginning of unload and reload cycle and it increases as the cycle progresses.

4.2.5 Castlegate Irrecoverable strain

The plot of confining pressure vs axial strain for Castlegate is shown Figure 4.17. The value of irrecoverable strain is approximately 16%.

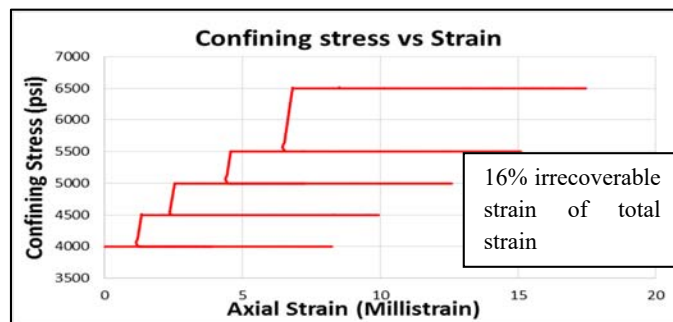


Figure 4.17: The confining pressure vs axial strain. The value of irrecoverable strain is approximately 16%.

4.3 Austin Chalk

The Austin Chalk is an upper cretaceous geologic formation in the Gulf Coast region of the United States. It is named after outcrops near Austin, Texas. The Austin Chalk consists of recrystallized, fossiliferous, interbedded chalks and marls (Weishampel, The dinosaurian). The Austin Chalk outcrops can be seen throughout Dallas extending into Austin and San Antonio. The depth of deposition of Austin Chalk occurred in 820 ft. of water, (Weishampel, The dinosauria). Figure 4.18 shows the posttest and pretest sample pictures. The sample measurements are shown in Table 4.3.

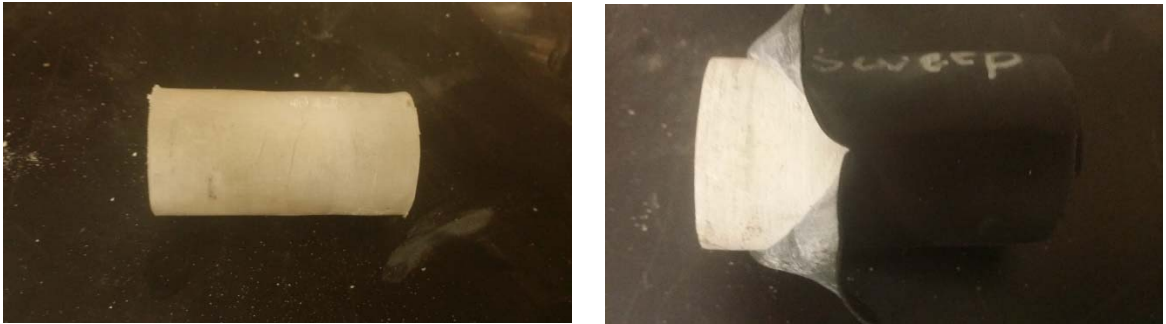


Figure 4.18: Austin chalk pretest and posttest sample picture. This sample exhibited a ductile failure.

Table 4.3: Austin Chalk sample measurements

Length	1.962 in
Diameter	0.986 in
Weight	51.55 g
Bulk density	1.88 g/cc

The fountain plot for the multistage test performed on Austin Chalk is shown in Figure 4.19. The test was run at confining pressures of 500, 2000, 3500, 5000 and 6500 psi. There is a significant effect of confining stress on the sample stiffness, larger than Castlegate but smaller than Berea. The nonlinearity near the PPD is larger than either

Castlegate or Berea. This is consistent with its highly ductile nature. The p/q plot for Austin Chalk is shown in Figure 4.20.

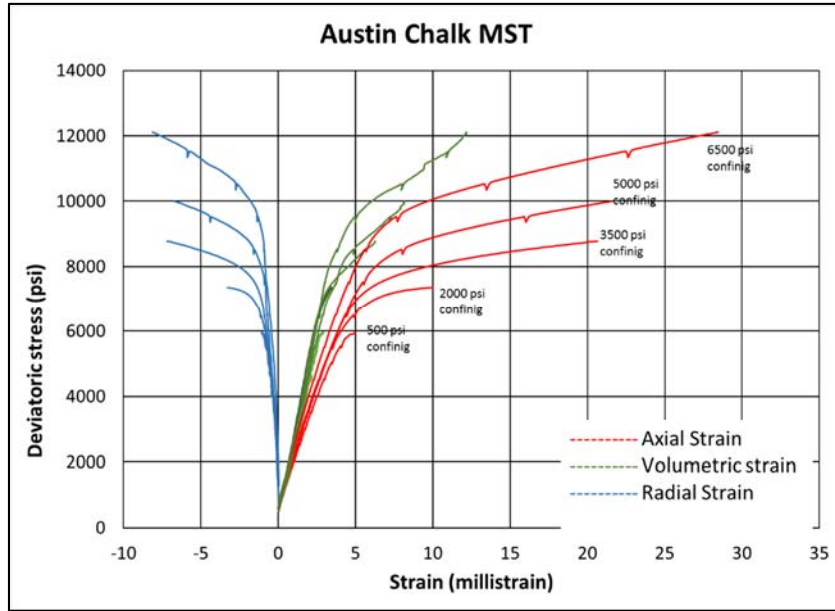


Figure 4.19: The Fountain plot for the multistage test performed on Austin Chalk showing radial, axial and volumetric strains. The sample exhibited very ductile behavior near the PPD.

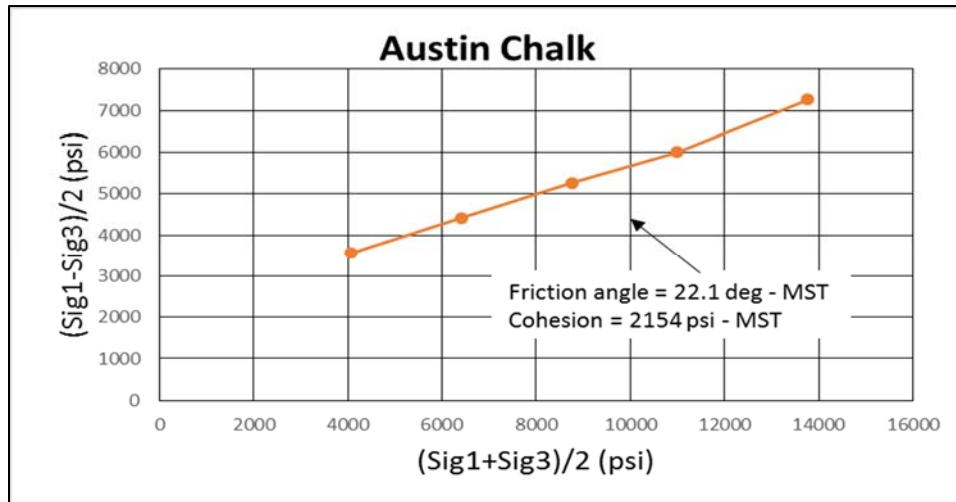


Figure 4.20: The p/q plot for Austin Chalk, the friction angle is 22.1 degrees and the measured cohesion is 2154 psi. Due to the ductile nature of this material the actual cohesion may be much lower (nonlinear yield criteria).

4.3.1 Static and Dynamic Young's Modulus - Austin Chalk

Figure 4.21 contains plots of static and dynamic Young's modulus versus axial strain for Austin chalk. M_1 is again the numerical derivative at the beginning of loading and unloading cycle.

Similar to other samples, the static modulus decreases with increasing deviatoric stress whereas dynamic modulus increases. At the start of unload stress path, we can see that static modulus is larger than dynamic modulus. The largest observed in any of these samples. This is interpreted as creep effects (time dependent strains) that are encountered at high axial stresses beyond axial yield point.

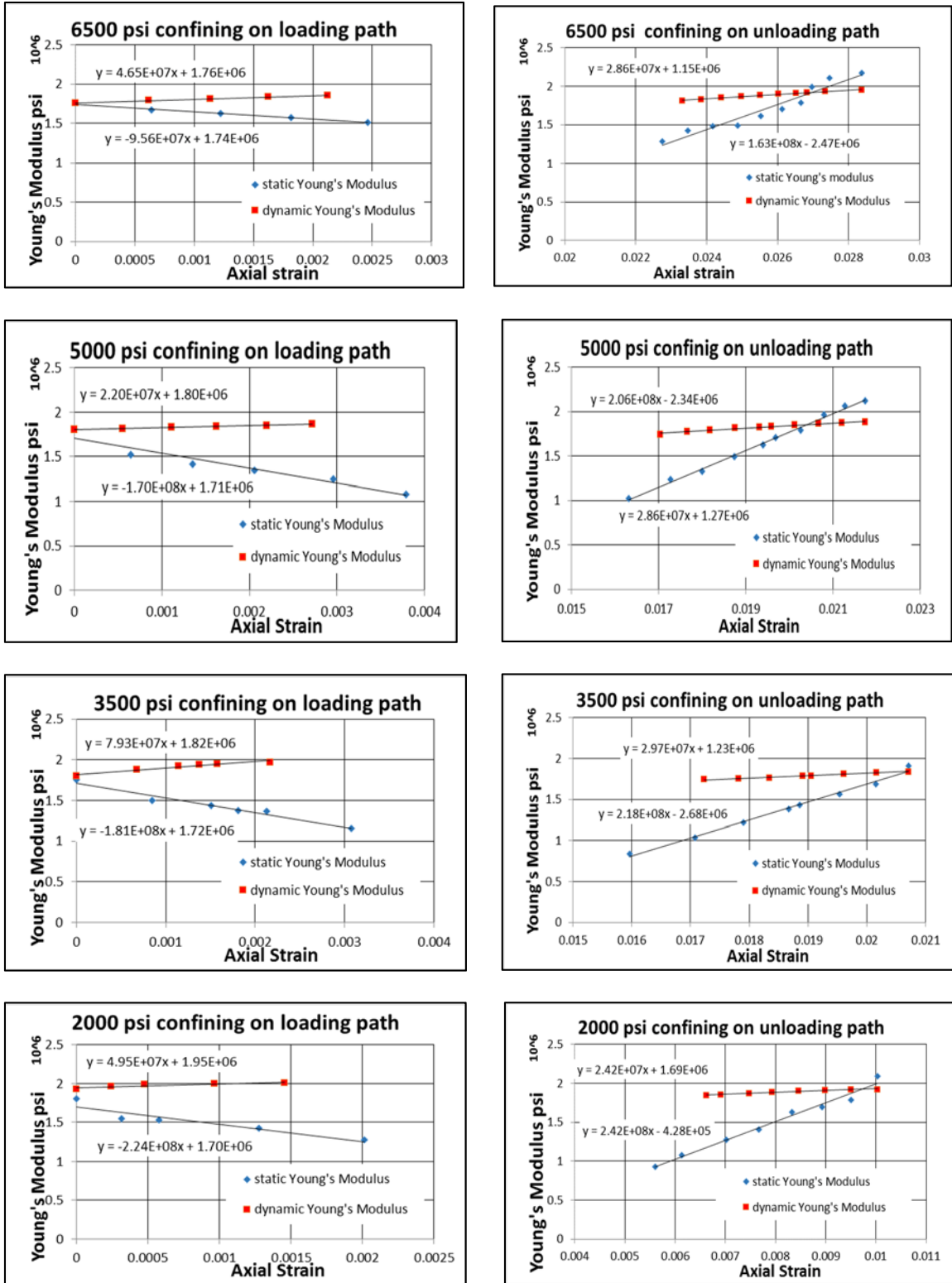


Figure 4.21 a, b: Static and dynamic Young's modulus versus strain on loading and unloading stress paths. The moduli at the beginning of the unloading stress path cross. This is interpreted as the effects of creep.

4.3.3 Austin Chalk Small Strain Young's Modulus

Similar to the samples above, Figure 4.22 a, b are plots of the static M_1 which were obtained from quadratic fits to the stress-strain data versus M_1 obtained from velocity data.

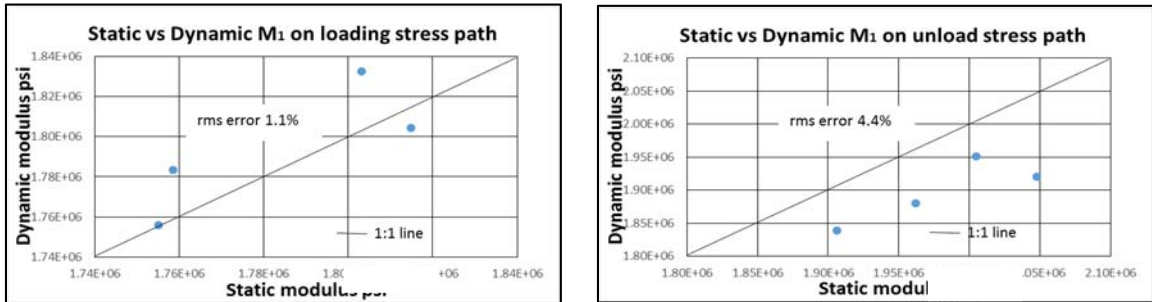


Figure 4.22 a, b: The static versus dynamic small strain modulus on loading and unloading stress paths. Both the moduli are equal to each other within the experimental error.

4.3.4 Austin Chalk Hypermodulus

Figure 4.23a and Figure 4.23b are plots of hypermodulus versus confining stress for both loading and unloading stress path on a semilog plot. With increasing confining pressure the value of M_2 decreases which means that sample is becoming more linear. The same affect was observed for the other samples.

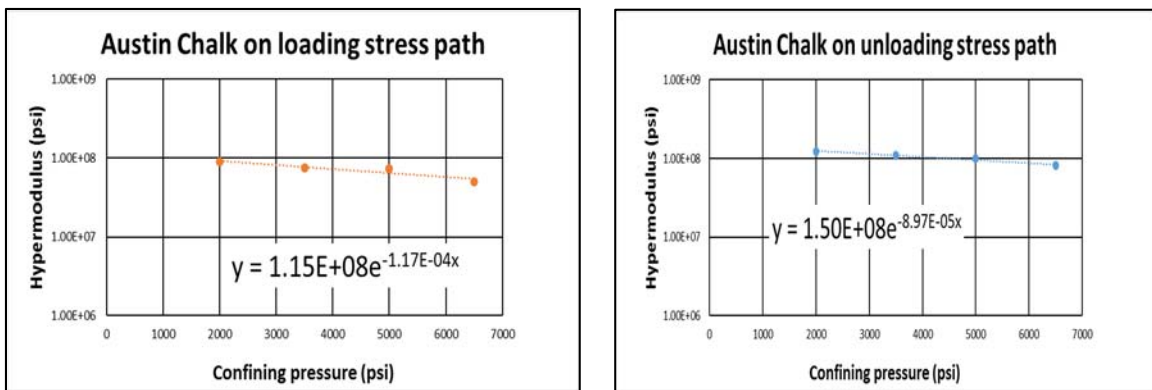


Figure 4.23 a, b: Hypermodulus vs confining pressure for loading and unloading stress path

4.3.5 Austin Chalk Poisson's Ratio

The plot of Poisson's ratio for Austin Chalk as a function of deviatoric stress on both loading and unloading stress path are shown in figure 4.24a and 4.24b.

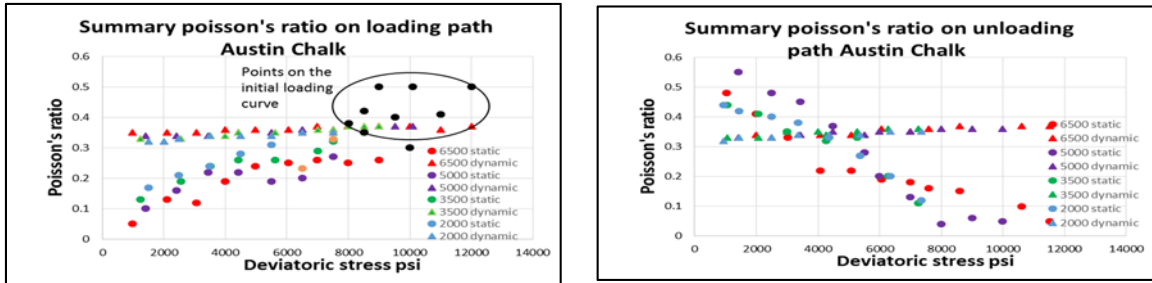


Figure 4.24 a, b: Austin Chalk Poisson's ratio on loading and unloading stress path respectively plotted for different confining pressures.

Similar to other samples at the beginning of both loading and unloading cycle the Poisson's ratio is small and increases with changes in deviatoric stress. The dynamic Poisson's ratio on the other hand is nearly constant.

4.3.5 Austin Chalk Irrecoverable Strains

Figure 4.25 is graph of confining pressure vs axial strain. This plot is used to measure irrecoverable strains directly.

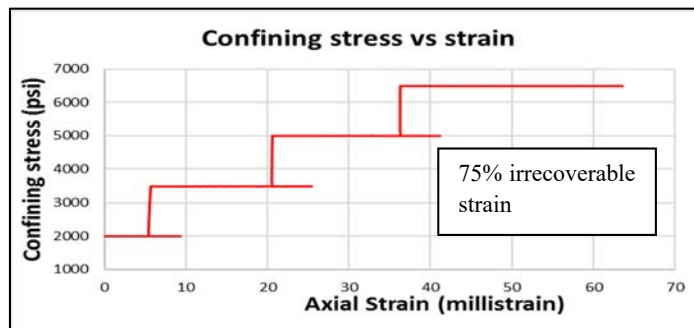


Figure 4.25: Confining pressure vs axial strain to calculate irrecoverable strains directly. The measured value of irrecoverable strain is 75%.

4.4 Dundee Sandstone

Dundee sandstone is similar to Berea Sandstone and is from the Massillon formation in Pennsylvania. While having similar porosities and bulk densities to Berea Sandstone, Dundee is laminated and more permeable, with permeability in the range of 900mD-2500mD (large grains). The pretest and posttest sample pictures are shown in Figure 4.26. The sample measurements are given in table 4.4.

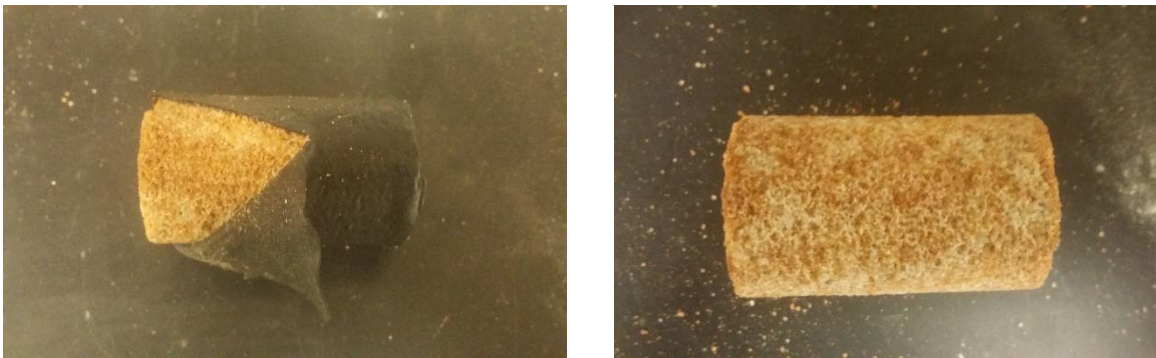


Figure 4.26: Posttest and pretest sample picture. The sample is kept in viton sleeve post test to keep it intact. The slip surface is evident in the post test picture. This sample exhibited a brittle behavior.

Table 4.4: Dundee sample measurements

Length	1.951 in
Diameter	1.016 in
Weight	52.288 g
Bulk density	2.02 g/cc

Figure 4.27 is the fountain plot for the multistage triaxial test. The tests were run at 100, 500 and 1000 psi confining stress.

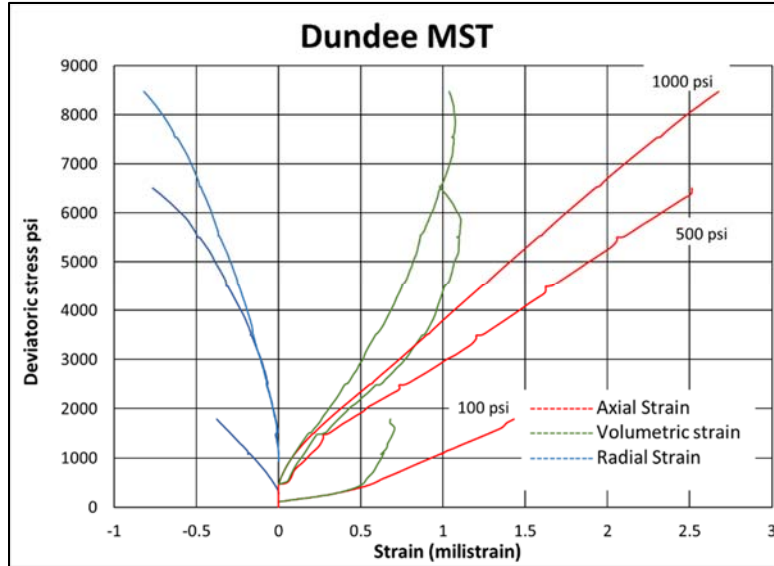


Figure 4.27: Fountain plot for multistage tri-axial test for Dundee.

The plot of stress-strain is linear throughout the whole range till the PPD. We will later see very large recoverable strains which is due to elastic deformation. There is a large effect of confining pressure on the sample stiffness.

The Mohr Coulomb plot to calculate friction angle and cohesion is shown in Figure 4.28. The friction angle from the plot is 54.8 degrees the largest measured value. The cohesion is 222.3 psi, the lowest value measured.

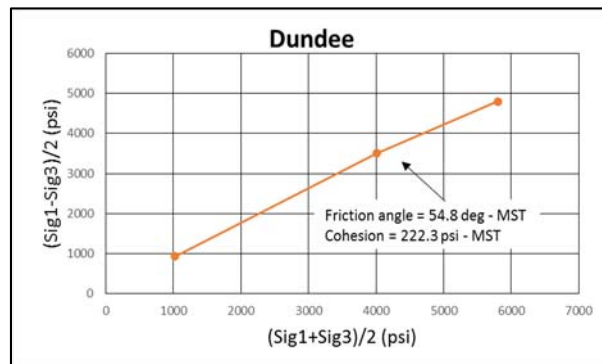


Figure 4.28: Mohr Coulomb plot for Dundee showing friction angle of 54.8 deg and 222.3 psi cohesion.

4.4.1 Interpretation of Static and Dynamic Young's Modulus Measurements

In this section we will look at the effect of increasing deviatoric stress on both static and dynamic Young's modulus. Figure 4.29 a, b is plot of Young's modulus vs strain for confining pressure of 1000 and 500 psi. As expected the static modulus decreases whereas dynamic modulus increases with increasing deviatoric stress and strain.

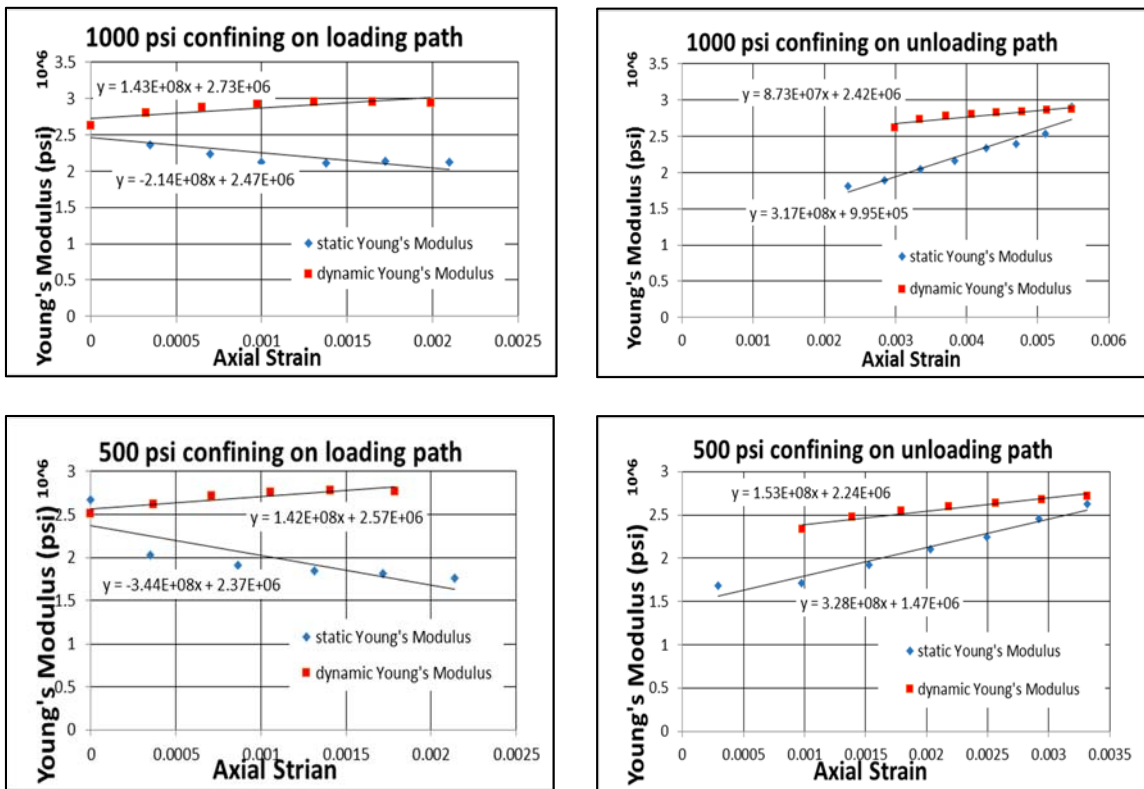


Figure 4.29 a, b: Static and dynamic Young's modulus versus strain on loading and unloading stress paths.

4.4.2 Dundee small strain young's modulus (M_1)

The static M_1 modulus versus dynamic modulus is shown in Figure 4.30 a, b. Both static and dynamic M_1 are equal to each other within the experimental error. The

static M_1 is obtained from quadratic fit to the static data. Dynamic M_1 is obtained from the velocities at the beginning of unload and reload stress path.

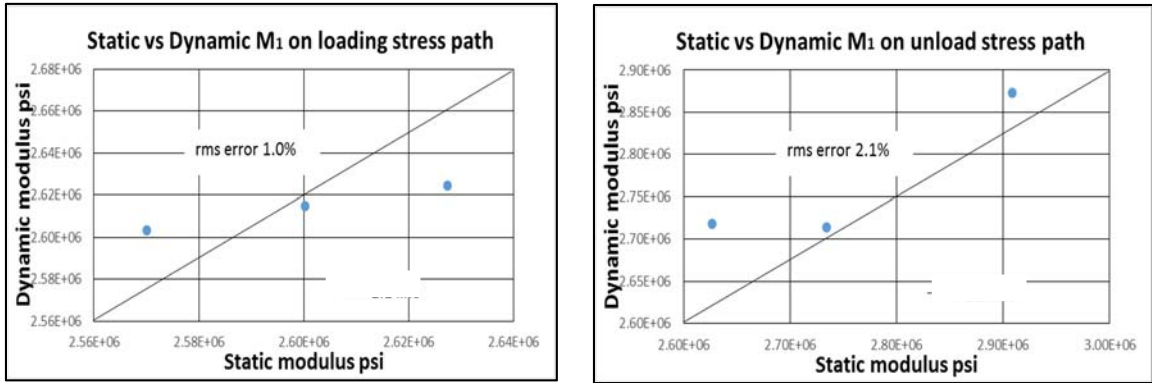


Figure 4.30 a, b: The static versus dynamic moduli on the loading and unloading stress path.

4.4.3 Dundee Hypermodulus

Figure 4.31a and Figure 4.31b are plots of the hypermodulus versus confining pressure for both loading and unloading stress path. The hypermodulus decreases as the test progresses to larger confining stress and sample damage for both loading and unloading stress path.

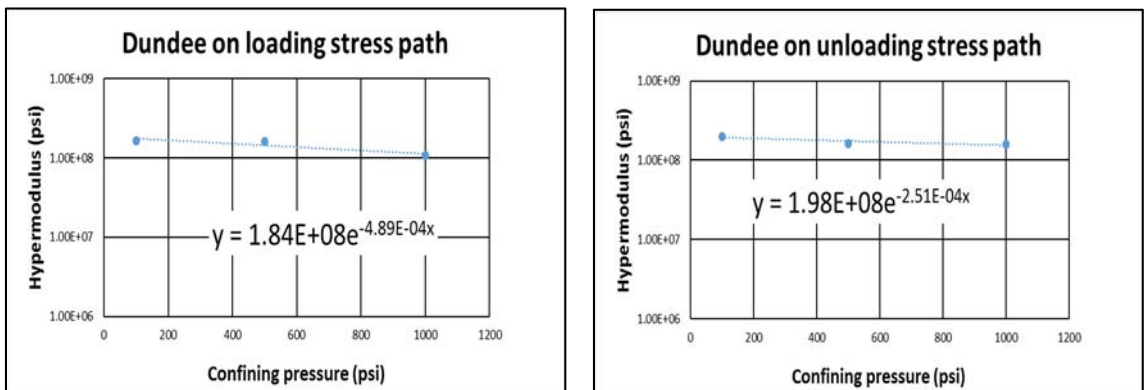


Figure 4.31 a, b: Hypermodulus vs confining pressure for loading and unloading cycle respectively

4.4.5 Dundee Irrecoverable Strains

Figure 4.32 is plot of confining pressure vs strain to axial strain to calculate irrecoverable strain directly. The average irrecoverable strain is only 10%. The values are tabulated in appendix.

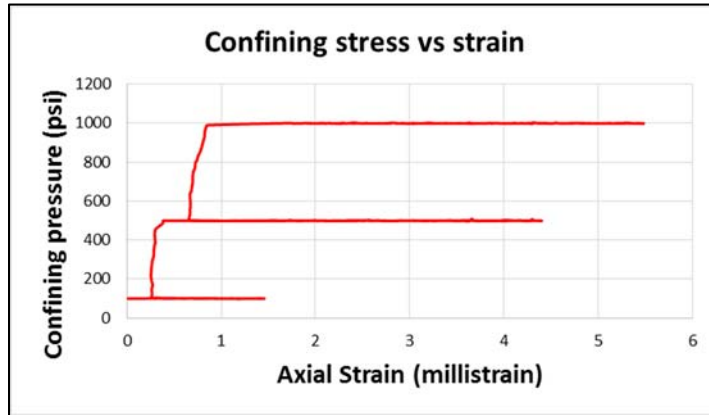


Figure 4.32 Confining pressure vs axial strain to calculate irrecoverable strains directly

Chapter 5 - Results

5.1 Hypermodulus versus confining pressure

Figure 5.1a and figure 5.1b are semilog plots of hypermodulus for all the samples plotted as a function of confining pressure on both loading and unloading stress path.

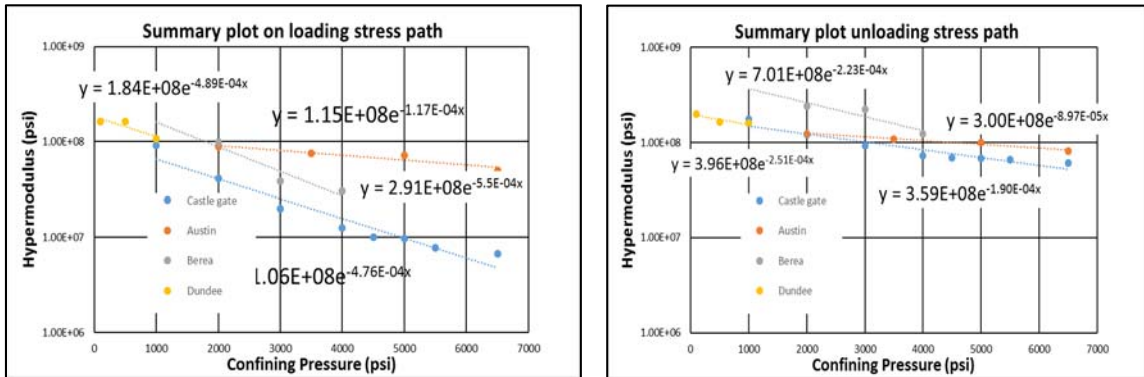


Figure 5.1: a, b Hyper modulus vs confining pressure for all the samples.

For all of the samples in Figure 5.1 the M_2 decreases with increasing confining pressure. This change is also correlated to the increased sample damage, cracking etc. that occurs as the sample loading increases. As discussed in section 5.3 we believe this is the key to the stress dependence shown above.

5.2 Summary plot for M_1

In figure 5.2 we are plotting dynamic M_1 obtained from velocity against the static M_1 obtained from the quadratic fit to the data for the four different rocks that we have tested.

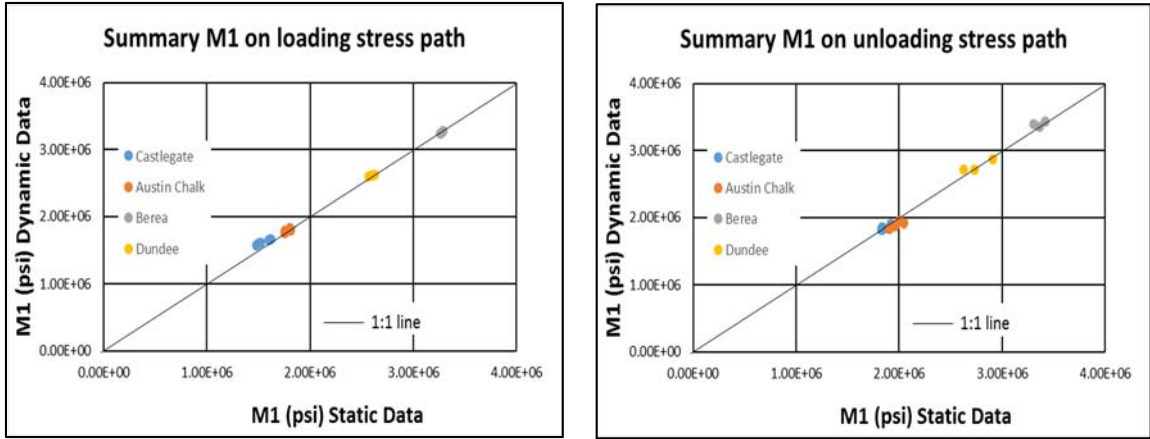


Figure 5.2: Static M_1 vs dynamic M_1 for all the rocks. They are equal within experimental error.

In figure 5.3 we have plotted the M_1 values obtained from quadratic fits against the M_1 values obtained from numerical computation. They are approximately similar as can be seen in the plot.

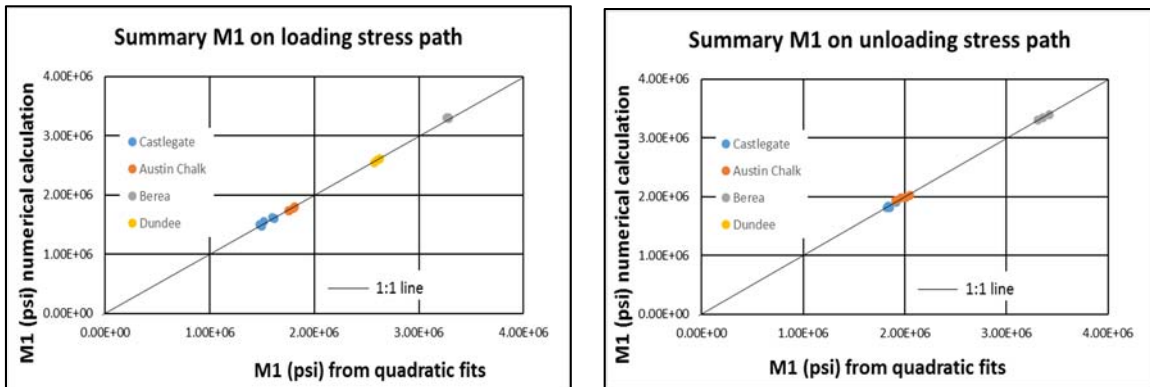


Figure 5.3: Comparison of M_1 obtained from quadratic fits vs M_1 obtained from numerical calculations.

5.3 Relation between irrecoverable strain and hypermodulus

Figures 5.1 we saw that the different samples have different value for exponential slope. In Figures 5.4 we have plotted the value of the exponential slope against the average irrecoverable strain for each rock.

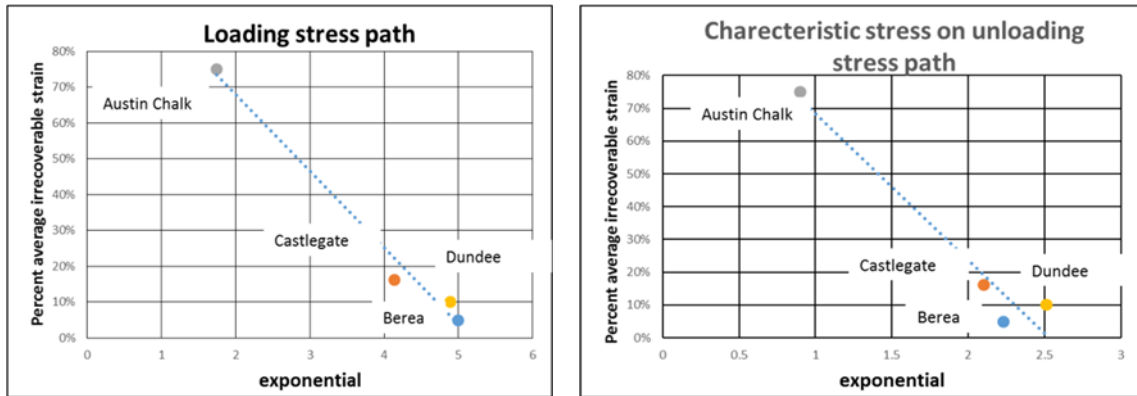


Figure 5.4: Percent irrecoverable strain vs exponential for different rocks

The plots in figure 5.4 show that for all the samples the hypermodulus decreases with increasing confining stress following a single trend.

5.3 Conceptual Model

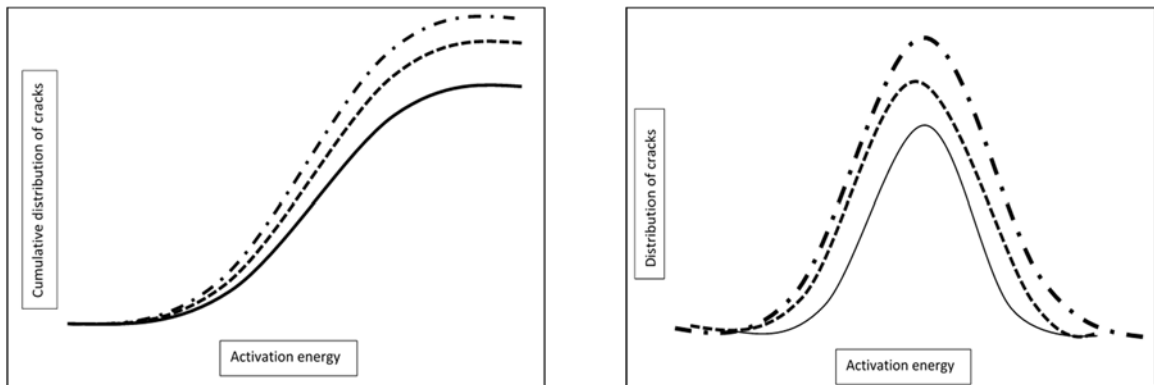


Figure 5.5 Conceptual model to explain Poisson's ratio and Young's modulus as a function of sample damage.

In Figure 5.5 we show a cartoon of the model that we propose to explain the behavior of the static and dynamic moduli and Poisson's ratio. Depending on the rocks mineralogy, texture and stress history there exists a distribution of compliant pores which will open as a function of their "activation stress" at the beginning of either the loading or unloading stress cycle only the wings of the distribution are involved and only a small

number of compliant pores are opening or closing. Young's modulus will therefore be equal for the velocity and static data at small strains. As the loading or unloading proceeds the number of pores involved increases and the pores already activated continue to contribute. It is the cumulative distribution that will control the rocks response. The static Young's modulus will therefore decrease while the dynamic modulus will increase.

Poisson's ratio behaves differently because its magnitude is controlled by the strain orthogonal to the applied loading parameter. At the start of the static measurement Poisson's ratio is very small since there are very few compliant pores that are contributing to the lateral expansion. Poisson's ratio increases with increasing load on the reloading cycle and decrease with unloading. The different curves sketched in Figure 5.5 are meant to show the effect of the increased sample damage associated with the initial loading curve. M_2 is expected to be inversely correlated with the area under this curve i.e. with the accumulated sample damage. The mathematical model associated with Figure 5.5 and its calibration will be the focus of future work.

5.4 Conclusions

The static and dynamic moduli of four samples were measured. These data are tabulated in the appendix. The samples ranged in static modulus from $3 \cdot 10^6$ psi to $7 \cdot 10^5$ psi, irrecoverable strain from 5% to 90%, and the measured velocity ranged from $1.4 \cdot 10^4$ in/s to $1.0 \cdot 10^4$ in/s. Based on these measurements we have observed the following:

- The dynamic Young's modulus is greater than or equal to the static modulus. They are equal at the beginning of both the unloading or reloading cycle.
- The difference between the static and dynamic moduli increases as the reload and unload cycle progresses.
- The static and dynamic moduli derived from an unloading or reloading cycle are accurately fit with two parameters (M_1 & M_2) where M_1 is obtained from velocity data and M_2 is inversely related to the level of irrecoverable strain.
- Poisson's ratio is close to zero at the beginning of an unloading or reloading cycle and equal to the dynamic value at the end of the cycle.
- The data is conceptually consistent with a simple distribution of compliant pores model for both Young's modulus and Poisson's ratio

We believe this is the first time a delineation of the separate mechanisms, i.e. linear versus nonlinear effects in elastic moduli has been reported and the mechanisms related to the velocity and the accumulated damage in a sample. This will allow future imaging work to quantify the mechanisms and ultimately allow the prediction of static moduli from a combination of micro CT, thin sections and SEM data with velocity measurements.

Chapter 6 Appendix

6.1 Berea Tabulated Data

Table 6.1 Berea measured data on loading stress path for 2000 psi confining stress.

Strain	Static YM	Dynamic YM	Vp (in/s)	Vs (in/s)
0.00E+00	3.26E+06	3.24E+06	1.40E+04	6.31E+03
3.43E-04	2.93E+06	3.28E+06	1.40E+04	6.31E+03
6.66E-04	2.84E+06	3.31E+06	1.42E+04	6.35E+03
8.59E-04	2.83E+06	3.35E+06	1.42E+04	6.45E+03
1.21E-03	2.80E+06	3.39E+06	1.43E+04	6.45E+03
1.57E-03	2.87E+06	3.40E+06	1.42E+04	6.50E+03
1.91E-03	2.71E+06	3.42E+06	1.41E+04	6.52E+03
2.24E-03	2.72E+06	3.42E+06	1.42E+04	6.56E+03
2.59E-03	2.58E+06	3.43E+06	1.41E+04	6.55E+03
2.98E-03	2.50E+06	3.43E+06	1.43E+04	6.60E+03
3.37E-03	2.37E+06	3.43E+06	1.43E+04	6.59E+03

Table 6.2 Berea data on unloading stress path for 2000 psi confining stress

Strain	Static YM	Dynamic YM	Vp (in/s)	Vs (in/s)
4.27E-03	3.36E+06	3.36E+06	1.41E+04	6.51E+03
3.97E-03	3.33E+06	3.34E+06	1.41E+04	6.46E+03
3.66E-03	3.26E+06	3.34E+06	1.41E+04	6.43E+03
3.34E-03	3.05E+06	3.33E+06	1.41E+04	6.41E+03
3.00E-03	2.75E+06	3.33E+06	1.41E+04	6.42E+03
2.61E-03	2.47E+06	3.31E+06	1.40E+04	6.36E+03
2.18E-03	2.20E+06	3.28E+06	1.43E+04	6.40E+03
1.70E-03	1.97E+06	3.23E+06	1.43E+04	6.40E+03
1.15E-03	1.70E+06	3.23E+06	1.43E+04	6.35E+03
9.15E-04	1.63E+06	3.24E+06	1.42E+04	6.33E+03
6.69E-04	1.55E+06	3.24E+06	1.42E+04	6.30E+03
2.32E-04	1.25E+06	3.24E+06	1.42E+04	6.30E+03

Table 6.3 Berea data values on loading stress path for 3000 psi confining stress

Strain	Static YM	Dynamic YM	Vp (in/s)	Vs (in/s)
0.00E+00	3.29E+06	3.24E+06	1.40E+04	6.27E+03
3.40E-04	3.04E+06	3.28E+06	1.40E+04	6.31E+03
6.60E-04	3.10E+06	3.31E+06	1.41E+04	6.36E+03
7.86E-04	3.01E+06	3.43E+06	1.41E+04	6.47E+03
1.11E-03	3.04E+06	3.46E+06	1.42E+04	6.49E+03
1.43E-03	3.08E+06	3.48E+06	1.42E+04	6.50E+03
1.74E-03	3.08E+06	3.50E+06	1.41E+04	6.52E+03
2.06E-03	3.05E+06	3.51E+06	1.40E+04	6.56E+03
2.37E-03	3.02E+06	3.52E+06	1.41E+04	6.57E+03
2.65E-03	2.98E+06	3.53E+06	1.43E+04	6.59E+03
2.95E-03	2.95E+06	3.53E+06	1.43E+04	6.58E+03
3.27E-03	2.90E+06	3.54E+06	1.43E+04	6.59E+03
3.59E-03	2.83E+06	3.55E+06	1.44E+04	6.59E+03

Table 6.4 Berea Data on unloading stress path for 3000 psi confining stress

Strain	Static YM	Dynamic YM	Vp (in/s)	Vs (in/s)
4.87E-03	3.42E+06	3.44E+06	1.43E+04	6.48E+03
4.58E-03	3.42E+06	3.43E+06	1.43E+04	6.50E+03
4.28E-03	3.35E+06	3.43E+06	1.42E+04	6.50E+03
3.98E-03	3.32E+06	3.43E+06	1.42E+04	6.40E+03
3.66E-03	3.01E+06	3.42E+06	1.42E+04	6.42E+03
3.33E-03	3.00E+06	3.42E+06	1.41E+04	6.43E+03
2.98E-03	2.82E+06	3.41E+06	1.41E+04	6.42E+03
2.61E-03	2.55E+06	3.41E+06	1.41E+04	6.40E+03
2.19E-03	2.30E+06	3.41E+06	1.41E+04	6.39E+03
1.74E-03	2.16E+06	3.41E+06	1.41E+04	6.38E+03
1.34E-03	1.89E+06	3.40E+06	1.41E+04	6.37E+03
1.06E-03	1.84E+06	3.31E+06	1.41E+04	6.40E+03
5.67E-04	1.68E+06	3.28E+06	1.40E+04	6.36E+03
2.01E-04	1.59E+06	3.24E+06	1.40E+04	6.36E+03

Table 6.5 Berea data on loading stress path for 4000 psi confining stress

Strain	Static YM	Dynamic YM	Vp (in/s)	Vs (in/s)
0.00E+00	3.26E+06	3.24E+06	1.40E+04	6.26E+03
3.27E-04	3.25E+06	3.28E+06	1.40E+04	6.31E+03
5.70E-04	3.30E+06	3.31E+06	1.41E+04	6.36E+03
7.20E-04	3.28E+06	3.35E+06	1.41E+04	6.39E+03
1.04E-03	3.26E+06	3.39E+06	1.41E+04	6.42E+03
1.64E-03	3.26E+06	3.43E+06	1.42E+04	6.48E+03
1.92E-03	3.26E+06	3.44E+06	1.42E+04	6.48E+03
2.20E-03	3.24E+06	3.45E+06	1.42E+04	6.54E+03
2.48E-03	3.23E+06	3.46E+06	1.43E+04	6.54E+03
2.77E-03	3.22E+06	3.47E+06	1.43E+04	6.54E+03
3.03E-03	3.20E+06	3.48E+06	1.43E+04	6.54E+03

Table 6.6 Berea data on unloading stress path for 4000 psi confining stress

Strain	Static YM	Dynamic YM	Vp (in/s)	Vs (in/s)
5.16E-03	3.31E+06	3.45E+06	1.43E+04	6.53E+03
4.86E-03	3.30E+06	3.45E+06	1.42E+04	6.54E+03
4.55E-03	3.26E+06	3.44E+06	1.42E+04	6.51E+03
4.24E-03	3.17E+06	3.44E+06	1.43E+04	6.50E+03
3.92E-03	3.02E+06	3.44E+06	1.42E+04	6.50E+03
3.59E-03	3.03E+06	3.43E+06	1.42E+04	6.42E+03
3.26E-03	3.07E+06	3.43E+06	1.42E+04	6.42E+03
2.94E-03	3.02E+06	3.43E+06	1.41E+04	6.44E+03
2.60E-03	2.84E+06	3.44E+06	1.41E+04	6.42E+03
2.24E-03	2.72E+06	3.43E+06	1.41E+04	6.40E+03
1.85E-03	2.64E+06	3.41E+06	1.41E+04	6.39E+03
1.63E-03	2.55E+06	3.37E+06	1.41E+04	6.38E+03
1.21E-03	2.56E+06	3.35E+06	1.41E+04	6.37E+03
9.97E-04	2.39E+06	3.31E+06	1.41E+04	6.42E+03
6.16E-04	2.18E+06	3.28E+06	1.40E+04	6.36E+03

Table 6.7: Summary table for M1 and M2 as a function of stress for Berea

Confining pressure	Loading		Unloading	
	M ₁	M ₂	M ₁	M ₂
2000	3.22e6	9.90e7	3.33e6	2.39e8
3000	3.26e6	3.81e7	3.40e6	2.20e8
4000	3.26e6	1.08e7	3.33e6	1.25 e8

Table 6.8: Percent irrecoverable strain at each confining pressure.

Confining pressure	Percent irrecoverable strain
4000	5.1
3000	4.7
2000	5.3

6.2 Castlegate

Table 6.9 Castlegate data for 6500 psi confining on loading stress path

Strain	Static YM	Dynamic YM	Vp (in/s)	Vs (in/s)
0.00E+00	1.45E+06	1.41E+06	9.83E+03	4.64E+03
6.94E-04	1.40E+06	1.51E+06	9.88E+03	4.74E+03
1.41E-03	1.36E+06	1.60E+06	9.90E+03	4.84E+03
2.14E-03	1.39E+06	1.68E+06	1.00E+04	4.86E+03
2.85E-03	1.38E+06	1.74E+06	1.05E+04	4.96E+03
3.58E-03	1.37E+06	1.80E+06	1.05E+04	4.96E+03
4.34E-03	1.35E+06	1.81E+06	1.05E+04	4.96E+03
5.06E-03	1.33E+06	1.82E+06	1.07E+04	4.97E+03
5.85E-03	1.31E+06	1.85E+06	1.08E+04	4.98E+03

Table 6.10 Castlegate data for 6500 psi confining on unloading stress path

Strain	Static	Dynamic YM	Vp (in/s)	Vs (in/s)
9.82E-03	1.85E+06	1.83E+06	1.08E+04	4.98E+03
9.28E-03	1.70E+06	1.81E+06	1.07E+04	4.98E+03
8.65E-03	1.65E+06	1.79E+06	1.05E+04	4.97E+03
8.46E-03	1.56E+06	1.78E+06	1.06E+04	4.95E+03
8.00E-03	1.54E+06	1.77E+06	1.03E+04	4.97E+03
7.71E-03	1.48E+06	1.77E+06	1.08E+04	4.98E+03
7.06E-03	1.41E+06	1.79E+06	1.05E+04	4.96E+03
6.28E-03	1.31E+06	1.77E+06	1.04E+04	4.93E+03
5.49E-03	1.21E+06	1.76E+06	1.04E+04	4.90E+03
4.66E-03	1.17E+06	1.74E+06	1.02E+04	4.80E+03
3.74E-03	1.07E+06	1.72E+06	1.00E+04	4.86E+03

Table 6.11 Castlegate data for 5500 psi confining on loading stress path

Strain	Static YM	Dynamic YM	Vp (in/s)	Vs (in/s)
0.00E+00	1.49E+06	1.62E+06	9.63E+03	4.74E+03
6.88E-04	1.42E+06	1.66E+06	9.64E+03	4.77E+03
1.40E-03	1.36E+06	1.70E+06	9.64E+03	4.86E+03
2.13E-03	1.40E+06	1.74E+06	9.66E+03	4.94E+03
2.87E-03	1.38E+06	1.78E+06	9.71E+03	4.96E+03
4.33E-03	1.34E+06	1.81E+06	9.66E+03	4.98E+03
5.12E-03	1.33E+06	1.84E+06	9.81E+03	4.94E+03
5.88E-03	1.30E+06	1.86E+06	1.06E+04	5.06E+03

Table 6.12 Castlegate data for 5500 psi confining on unloading stress path

Strain	Static YM	Dynamic YM	Vp (in/s)	Vs (in/s)
1.01E-02	1.82E+06	1.83E+06	1.09E+04	4.98E+03
9.91E-03	1.77E+06	1.82E+06	1.06E+04	4.97E+03
9.60E-03	1.72E+06	1.81E+06	1.06E+04	4.95E+03
9.33E-03	1.71E+06	1.80E+06	1.02E+04	4.97E+03
8.99E-03	1.62E+06	1.79E+06	1.03E+04	4.98E+03
8.69E-03	1.58E+06	1.78E+06	1.04E+04	4.96E+03
8.40E-03	1.57E+06	1.77E+06	1.04E+04	4.93E+03
7.86E-03	1.46E+06	1.77E+06	1.04E+04	4.90E+03
7.69E-03	1.48E+06	1.75E+06	1.03E+04	4.80E+03
7.36E-03	1.41E+06	1.70E+06	1.00E+04	4.86E+03
7.02E-03	1.31E+06	1.69E+06	9.80E+03	4.86E+03
6.50E-03	1.31E+06	1.68E+06	9.75E+03	4.86E+03
5.11E-03	1.11E+06	1.66E+06	9.73E+03	4.86E+03
4.21E-03	1.05E+06	1.64E+06	9.70E+03	4.86E+03
3.23E-03	9.63E+05	1.62E+06	9.64E+03	4.77E+03

Table 6.13 Castlegate data for 5000 psi confining on loading stress path

Strain	Static YM	Dynamic YM	Vp (in/s)	Vs (in/s)
0.00E+00	1.52E+06	1.66E+06	9.63E+03	4.74E+03
7.04E-04	1.46E+06	1.69E+06	9.62E+03	4.76E+03
1.43E-03	1.39E+06	1.72E+06	9.60E+03	4.84E+03
2.14E-03	1.37E+06	1.75E+06	9.65E+03	4.93E+03
2.87E-03	1.39E+06	1.77E+06	9.71E+03	4.94E+03
3.58E-03	1.37E+06	1.78E+06	9.70E+03	4.98E+03
4.34E-03	1.33E+06	1.80E+06	9.81E+03	4.96E+03
5.09E-03	1.31E+06	1.82E+06	1.04E+04	5.10E+03

Table 6.14 Castlegate data for 5000 psi confining on unloading stress path

Strain	Static YM	Dynamic YM	Vp (in/s)	Vs (in/s)
9.82E-03	1.92E+06	1.86E+06	1.08E+04	4.98E+03
9.58E-03	1.84E+06	1.85E+06	1.09E+04	4.97E+03
9.39E-03	1.82E+06	1.84E+06	1.05E+04	4.96E+03
9.13E-03	1.77E+06	1.83E+06	1.06E+04	4.95E+03
8.85E-03	1.67E+06	1.82E+06	1.03E+04	4.97E+03
8.64E-03	1.66E+06	1.81E+06	1.03E+04	4.98E+03
8.36E-03	1.61E+06	1.80E+06	1.04E+04	4.97E+03
7.89E-03	1.58E+06	1.79E+06	1.05E+04	4.92E+03
7.58E-03	1.52E+06	1.74E+06	1.04E+04	4.90E+03
7.47E-03	1.48E+06	1.73E+06	1.02E+04	4.80E+03
6.88E-03	1.38E+06	1.72E+06	1.00E+04	4.85E+03
6.24E-03	1.31E+06	1.71E+06	9.80E+04	4.86E+03
5.36E-03	1.20E+06	1.69E+06	9.73E+04	4.85E+03
4.49E-03	1.11E+06	1.67E+06	9.73E+03	4.84E+03
3.56E-03	1.02E+06	1.65E+06	9.70E+04	4.83E+03
2.52E-03	9.04E+05	1.63E+06	9.64E+03	4.77E+03

Table 6.15 Castlegate data for 4500 psi confining on loading stress path

Strain	Static YM	Dynamic YM	Vp (in/s)	Vs (in/s)
0.00E+00	1.48E+06	1.58E+06	9.62E+03	4.74E+03
6.98E-04	1.43E+06	1.65E+06	9.62E+03	4.77E+03
1.41E-03	1.39E+06	1.72E+06	9.59E+03	4.84E+03
2.13E-03	1.40E+06	1.77E+06	9.64E+03	4.90E+03
3.22E-03	1.36E+06	1.80E+06	9.73E+03	4.93E+03
3.94E-03	1.35E+06	1.84E+06	9.70E+03	4.96E+03
4.73E-03	1.31E+06	1.87E+06	9.81E+03	4.95E+03
5.92E-03	1.22E+06	1.91E+06	1.02E+04	5.08E+03

Table 6.16 Castlegate data for 4500 psi confining on unloading stress path

Strain	Static YM	Dynamic YM	Vp (in/s)	Vs (in/s)
8.20E-03	1.83E+06	1.86E+06	1.10E+04	4.97E+03
7.93E-03	1.80E+06	1.85E+06	1.04E+04	4.95E+03
7.65E-03	1.68E+06	1.83E+06	1.05E+04	4.95E+03
7.56E-03	1.73E+06	1.83E+06	1.03E+04	4.97E+03
7.03E-03	1.57E+06	1.81E+06	1.03E+04	4.97E+04
6.73E-03	1.56E+06	1.80E+06	1.02E+04	4.95E+03
6.47E-03	1.54E+06	1.79E+06	1.04E+04	4.92E+03
6.39E-03	1.44E+06	1.79E+06	1.04E+04	4.90E+03
5.70E-03	1.40E+06	1.78E+06	1.02E+04	4.85E+03
5.37E-03	1.36E+06	1.77E+06	1.00E+04	4.85E+03
5.23E-03	1.37E+06	1.77E+06	9.90E+04	4.86E+03
4.45E-03	1.26E+06	1.79E+06	9.83E+04	4.85E+03
3.60E-03	1.16E+06	1.77E+06	9.73E+03	4.84E+03
2.67E-03	1.06E+06	1.74E+06	9.70E+04	4.80E+03
1.68E-03	9.43E+05	1.72E+06	9.66E+03	4.77E+03

Table 6.17 Castlegate data for 4000 psi confining on loading stress path

Strain	Static YM	Dynamic YM	Vp (in/s)	Vs (in/s)
4.00E-05	1.50E+06	1.66E+06	9.62E+03	4.74E+03
7.15E-04	1.41E+06	1.71E+06	9.62E+03	4.74E+03
1.43E-03	1.39E+06	1.76E+06	9.60E+03	4.81E+03
2.16E-03	1.41E+06	1.81E+06	9.66E+03	4.85E+03
2.88E-03	1.37E+06	1.83E+06	9.73E+03	4.93E+03
3.61E-03	1.35E+06	1.86E+06	9.70E+03	4.96E+03
4.36E-03	1.32E+06	1.89E+06	9.81E+03	4.95E+03
5.14E-03	1.26E+06	1.91E+06	1.02E+04	5.04E+03

Table 6.18 Castlegate data for 4000 psi confining on unloading stress path

Strain	Static YM	Dynamic YM	Vp (in/s)	Vs (in/s)
7.86E-03	1.84E+06	1.85E+06	1.10E+04	4.97E+03
7.59E-03	1.74E+06	1.84E+06	1.04E+04	4.96E+03
7.30E-03	1.67E+06	1.83E+06	1.05E+04	4.95E+03
6.73E-03	1.58E+06	1.81E+06	1.03E+04	4.99E+03
6.37E-03	1.53E+06	1.80E+06	1.03E+04	4.97E+04
6.05E-03	1.50E+06	1.79E+06	1.02E+04	4.95E+03
5.85E-03	1.43E+06	1.78E+06	1.05E+04	4.90E+03
5.33E-03	1.35E+06	1.78E+06	1.04E+04	4.90E+03
4.94E-03	1.27E+06	1.78E+06	1.02E+04	4.85E+03
4.14E-03	1.20E+06	1.77E+06	1.00E+04	4.85E+03
3.47E-03	1.12E+06	1.75E+06	9.90E+04	4.86E+03
2.32E-03	1.04E+06	1.73E+06	9.83E+04	4.85E+03
1.31E-03	9.17E+05	1.72E+06	9.74E+03	4.84E+03

Table 6.19 Castlegate data for 3000 psi confining on both loading and unloading stress path (velocity data was not acquired)

loading		unloading	
strain	static YM	strain	static YM
5.88E-05	1.47E+06	6.71E-03	1.87E+06
7.29E-04	1.37E+06	6.14E-03	1.66E+06
1.55E-03	1.34E+06	5.53E-03	1.54E+06
2.31E-03	1.33E+06	4.81E-03	1.40E+06
3.03E-03	1.30E+06	4.11E-03	1.29E+06
3.78E-03	1.26E+06	3.28E-03	1.16E+06
4.55E-03	1.16E+06	2.42E-03	1.04E+06

Table 6.20 Castlegate data for 2000 psi confining on both loading and unloading stress path (velocity data was not acquired)

loading		unloading	
strain	static YM	strain	static YM
0.00E+00	1.43E+06	5.20E-03	1.72E+06
8.57E-04	1.28E+06	4.61E-03	1.53E+06
1.66E-03	1.26E+06	3.92E-03	1.38E+06
2.52E-03	1.21E+06	3.33E-03	1.25E+06
3.20E-03	1.14E+06	3.02E-03	1.18E+06
4.34E-03	9.33E+05		

Table 6.21 Castlegate data for 1000 psi confining on both loading and unloading stress path (velocity data was not acquired)

loading		unloading	
strain	static YM	strain	static YM
0.00E+00	1.49E+06	5.20E-03	1.62E+06
8.64E-04	1.08E+06	4.61E-03	1.43E+06
1.87E-03	8.83E+05	3.92E-03	1.21E+06
3.34E-03	7.10E+05	3.33E-03	1.06E+06
		3.02E-03	9.05E+05

Table 6.22: Summary table for Castlegate on loading stress path. For 1000, 2000 & 3000 psi confining the velocity data could not be acquired due to equipment failure

Confining	Loading		Unloading	
	M ₁	M ₂	M ₁	M ₂
1000		9.95e8		1.72e8
2000		5.11e7		1.20e8
3000		2.80e7		9.22e7
4000	1.60e6	1.90e7	1.80e6	7.27e7
4500	1.45e6	1.85e7	1.82e6	6.90e7
5000	1.50e6	1.80e7	1.95e6	6.81e7
5500	1.50e6	9.90e6	1.85e6	6.55e7
6500	1.47e6	9.70e6	1.84e6	6.12e7

6.3 Austin Chalk Tabulated Data

Table 6.23 Austin Chalk static and dynamic data, 6500 psi, confining pressure on loading stress path

strain	static YM	dynamic YM	Vp (in/s)	Vs (in/s)
0.00E+00	1.76E+06	1.76E+06	1.05E+04	4.86E+03
6.38E-04	1.67E+06	1.79E+06	1.02E+04	4.94E+03
1.23E-03	1.62E+06	1.81E+06	1.03E+04	4.94E+03
1.82E-03	1.57E+06	1.84E+06	1.05E+04	4.95E+03
2.46E-03	1.51E+06	1.85E+06	1.07E+04	5.00E+03

Table 6.24 Austin Chalk static and dynamic data at 6500 psi confining pressure on unloading stress path

strain	static YM	dynamic YM	Vp (in/s)	Vs (in/s)
2.84E-02	2.18E+06	1.95E+06	1.12E+04	5.07E+03
2.75E-02	2.10E+06	1.93E+06	1.11E+04	5.04E+03
2.70E-02	1.99E+06	1.92E+06	1.10E+04	5.03E+03
2.67E-02	1.79E+06	1.91E+06	1.10E+04	5.02E+03
2.61E-02	1.70E+06	1.90E+06	1.07E+04	5.00E+03
2.55E-02	1.61E+06	1.89E+06	1.08E+04	5.02E+03
2.49E-02	1.49E+06	1.87E+06	1.07E+04	5.00E+03
2.42E-02	1.48E+06	1.85E+06	1.05E+04	4.95E+03
2.35E-02	1.42E+06	1.83E+06	1.03E+04	4.94E+03
2.27E-02	1.28E+06	1.81E+06	1.02E+04	4.92E+03

Table 6.25 Austin Chalk static and dynamic data at 5000 psi confining pressure on loading stress path

strain	static YM	dynamic YM	Vp (in/s)	Vs (in/s)
0.00E+00	1.81E+06	1.80E+06	1.05E+04	4.86E+03
6.46E-04	1.52E+06	1.82E+06	1.02E+04	4.94E+03
1.35E-03	1.42E+06	1.83E+06	1.04E+04	4.98E+03
2.05E-03	1.35E+06	1.84E+06	1.06E+04	4.98E+03
2.96E-03	1.25E+06	1.85E+06	1.09E+04	5.01E+03
3.79E-03	1.08E+06	1.86E+06	1.19E+04	5.02E+03

Table 6.26 Austin Chalk static and dynamic data at 5000 psi confining pressure on unloading stress path

strain	static	dynamic YM	Vp (in/s)	Vs (in/s)
2.17E-02	2.12E+06	1.88E+06	1.08E+04	5.06E+03
2.13E-02	2.06E+06	1.87E+06	1.09E+04	5.03E+03
2.08E-02	1.97E+06	1.86E+06	1.06E+04	5.03E+03
2.03E-02	1.79E+06	1.85E+06	1.07E+04	5.02E+03
1.97E-02	1.71E+06	1.83E+06	1.07E+04	5.00E+03
1.94E-02	1.62E+06	1.83E+06	1.04E+04	5.01E+03
1.87E-02	1.49E+06	1.82E+06	1.02E+04	4.96E+03
1.80E-02	1.33E+06	1.79E+06	1.01E+04	4.95E+03
1.73E-02	1.24E+06	1.77E+06	1.00E+04	4.94E+03
1.63E-02	1.02E+06	1.74E+06	1.00E+04	4.90E+03

Table 6.27 Austin Chalk static and dynamic data at 3500 psi confining pressure on loading stress path

strain	static YM	dynamic YM	Vp (in/s)	Vs (in/s)
0.00E+00	1.76E+06	1.80E+06	1.05E+04	4.86E+03
8.49E-04	1.50E+06	1.88E+06	1.02E+04	4.94E+03
1.51E-03	1.44E+06	1.92E+06	1.04E+04	4.98E+03
1.81E-03	1.38E+06	1.94E+06	1.11E+04	5.07E+03
2.13E-03	1.37E+06	1.95E+06	1.12E+04	5.07E+03
3.07E-03	1.16E+06	1.97E+06	1.14E+04	5.06E+03

Table 6.28 Austin Chalk static and dynamic data at 3500 psi confining pressure on unloading stress path

strain	static YM	dynamic YM	Vp (in/s)	Vs (in/s)
2.07E-02	1.91E+06	1.84E+06	1.08E+04	5.06E+03
2.02E-02	1.69E+06	1.83E+06	1.09E+04	5.04E+03
1.95E-02	1.56E+06	1.81E+06	1.06E+04	5.03E+03
1.89E-02	1.43E+06	1.79E+06	1.06E+04	5.01E+03
1.87E-02	1.38E+06	1.78E+06	1.05E+04	5.00E+03
1.79E-02	1.22E+06	1.76E+06	1.04E+04	5.00E+03
1.71E-02	1.03E+06	1.75E+06	1.02E+04	4.96E+03
1.60E-02	8.42E+05	1.74E+06	1.01E+04	4.93E+03

Table 6.29 Austin Chalk static and dynamic data at 2000 psi confining pressure on loading stress path

strain	static YM	dynamic YM	Vp (in/s)	Vs (in/s)
0.00E+00	1.80E+06	1.93E+06	1.11E+04	5.04E+03
3.14E-04	1.55E+06	1.96E+06	1.10E+04	5.03E+03
5.79E-04	1.53E+06	1.99E+06	1.10E+04	5.02E+03
1.28E-03	1.42E+06	2.00E+06	1.13E+04	5.11E+03
2.02E-03	1.27E+06	2.01E+06	1.13E+04	5.12E+03

Table 6.30 Austin Chalk static and dynamic data at 2000 psi confining pressure on unloading stress path

strain	static YM	dynamic YM	Vp (in/s)	Vs (in/s)
1.00E-02	2.09E+06	1.92E+06	1.12E+04	5.07E+03
9.51E-03	1.79E+06	1.92E+06	1.11E+04	5.04E+03
8.93E-03	1.69E+06	1.91E+06	1.10E+04	5.03E+03
8.33E-03	1.63E+06	1.90E+06	1.09E+04	5.02E+03
7.66E-03	1.40E+06	1.89E+06	1.07E+04	5.00E+03
7.03E-03	1.28E+06	1.87E+06	1.06E+04	4.99E+03
6.13E-03	1.07E+06	1.85E+06	1.07E+04	4.96E+03
5.60E-03	9.25E+05	1.84E+06	1.05E+04	4.95E+03

Table 6.31: Summary values for Austin Chalk on loading stress path obtained from quadratic fits

Confining	Loading		Unloading	
	M ₁	M ₂	M ₁	M ₂
6500	1.77e6	5.00e7	1.95e6	8.15e7
5000	1.74e6	7.22e7	1.90e6	1.00e8
3500	1.79e6	7.50e7	2.10e6	1.09e8
2000	1.72e6	8.85e7	2.15e6	1.24e8

Table 6.32: Percent irrecoverable strain at each confining pressure.

Confining pressure	Percent irrecoverable strain
6500	77
5000	80
3500	78
2000	65

6.4 Dundee Tabulated Data

Table 6.33 Dundee static and dynamic data at 1000 psi confining on loading stress path

strain	static YM	dynamic YM	Vp (in/s)	Vs (in/s)
0.00E+00	2.63E+06	2.62E+06	1.16E+04	5.58E+03
3.48E-04	2.36E+06	2.80E+06	1.25E+04	5.73E+03
6.97E-04	2.24E+06	2.88E+06	1.29E+04	5.80E+03
1.00E-03	2.12E+06	2.93E+06	1.32E+04	5.83E+03
1.38E-03	2.11E+06	2.95E+06	1.33E+04	5.85E+03
1.73E-03	2.14E+06	2.95E+06	1.33E+04	5.85E+03
2.10E-03	2.12E+06	2.94E+06	1.33E+04	5.85E+03

Table 6.34 Dundee static and dynamic data at 1000 psi confining on unloading stress path

strain	static YM	dynamic YM	Vp (in/s)	Vs (in/s)
5.48E-03	2.91E+06	2.87E+06	1.33E+04	5.77E+03
5.11E-03	2.53E+06	2.86E+06	1.33E+04	5.75E+03
4.70E-03	2.40E+06	2.84E+06	1.32E+04	5.73E+03
4.28E-03	2.34E+06	2.82E+06	1.32E+04	5.72E+03
3.83E-03	2.16E+06	2.80E+06	1.30E+04	5.70E+03
3.35E-03	2.04E+06	2.78E+06	1.28E+04	5.69E+03
2.85E-03	1.89E+06	2.73E+06	1.24E+04	5.66E+03
2.33E-03	1.81E+06	2.62E+06	1.16E+04	5.57E+03

Table 6.35 Dundee static and dynamic data at 500 psi confining on loading stress path

strain	static YM	dynamic YM	Vp (in/s)	Vs (in/s)
0.00E+00	2.67E+06	2.52E+06	1.23E+04	5.54E+03
3.52E-04	2.03E+06	2.62E+06	1.28E+04	5.62E+03
8.67E-04	1.91E+06	2.72E+06	1.30E+04	5.67E+03
1.31E-03	1.85E+06	2.76E+06	1.32E+04	5.67E+03
1.72E-03	1.81E+06	2.78E+06	1.32E+04	5.66E+03
2.14E-03	1.76E+06	2.76E+06	1.33E+04	5.60E+03

Table 6.36 Dundee static and dynamic data at 500 psi confining on unloading stress path

strain	static YM	dynamic YM	Vp (in/s)	Vs (in/s)
3.32E-03	2.63E+06	2.72E+06	1.33E+04	5.60E+03
2.92E-03	2.46E+06	2.68E+06	1.32E+04	5.56E+03
2.49E-03	2.24E+06	2.64E+06	1.30E+04	5.52E+03
2.03E-03	2.10E+06	2.59E+06	1.28E+04	5.48E+03
1.53E-03	1.93E+06	2.54E+06	1.25E+04	5.43E+03
9.78E-04	1.71E+06	2.48E+06	1.21E+04	5.37E+03
2.90E-04	1.68E+06	2.33E+06	1.11E+04	5.26E+03

Table 6.37: Summary table for Dundee on loading stress path

Confining	Loading		Unloading	
	M ₁	M ₂	M ₁	M ₂
100	2.57e6	1.59e8	2.91e6	2.00e8
500	2.60e6	1.64e8	2.65e6	1.64e8
1000	2.61e6	1.07e8	2.85e6	1.59e8

Table 6.38: Percent irrecoverable strain at each confining pressure.

Confining pressure	Percent irrecoverable strain
1000	12
500	9
100	11

Bibliography

- E. Fjaer, Holt, Stroisz (2015) “Static vs Dynamic Moduli: another piece in the puzzle”, ARMA conference 2015.
- Alsalman, M.E, Myers M.T. Aldin M (2015) “Comparison of Multi-Stage to Single-Stage Tri-Axial test”. ARMA conference.
- Larsen, Fjaer, Renlie (2000) “Static and dynamic Poisson’s ratio of weak sandstones” Pacific Rocks.
- A Taheri, K Tani (2008) “ Proposal of a new Multiple-Step loading Triaxial Compression Testing Method” ISRM International Symposium.
- Kovari, K and A. Tisa (1975) “Multiple failure state and strain controlled triaxial tests” Rock Mechanics.
- Hertz, H.R, 1896 “ On contact between elastic bodies” in Collected works, Vol 1, Leipzig Germany.
- Weishampel, David B.; Dodson, Peter; and Osmólska, Halszka (2004): The Dinosauria, 2nd, Berkeley: University of California Press
- Andrews, E. B., 1870, Report of progress in the second district: Ohio Geol. Survey (Rept. Progress, 1869), pt. 2, p. 55-135.